Compare Results

Old File:		New File:
old-ms.pdf	versus	**Bailey-WMT-revisions3.pdf**
38 pages (7.70 MB)		**38 pages (7.70 MB)**
12/15/22, 03:46:29		2/7/23, 13:55:28

Total Changes	Content		Styling and Annotations	
42	6	Replacements	2	Styling
	16	Insertions	0	Annotations
	18	Deletions		

Go to First Change (page 1)

Water mass transformation variability in the Weddell Sea in Ocean Reanalyses

Shanice Bailey[1], Spencer Jones[2], Ryan Abernathey[1], Arnold Gordon[1], and Xiaojun Yuan[3]

[1]Department of Earth & Environmental Sciences of Columbia University Lamont-Doherty Earth Observatory | Room 106 Geoscience Bldg. P.O. Box 1000 Palisades, NY 10964, United States of America

[2]Department of Oceanography at Texas A&M University | Eller O&M Building, College Station, TX 77843, United States of America

[3]Lamont Doherty Earth Observatory | P.O. Box 1000 - 61 Route 9W Palisades, NY 10964, United States of America

Correspondence: Shanice Bailey (stb2145@columbia.edu)

Abstract. This study investigates the variability of water mass transformation (WMT) within the Weddell Gyre (WG). The WG serves as a pivotal site for the meridional overturning circulation (MOC) and ocean ventilation because it is the primary origin of the largest volume of water mass in the global ocean, Antarctic Bottom Water (AABW). Recent mooring data suggest substantial seasonal and interannual variability of AABW properties exiting the WG, and studies have linked the variability to

5   the large-scale climate forcings affecting wind stress in the WG region. However, the specific thermodynamic mechanisms that link variability in surface forcings to variability in water mass transformations and AABW export remain unclear. This study explores WMT variability via WMT volume budgets derived from Walin's classic WMT framework, using three state-of-the-art, data-assimilating ocean reanalyses: Estimating the Circulation and Climate of the Ocean state estimate (ECCOv4), Southern Ocean State Estimate (SOSE) and Simple Ocean Data Assimilation (SODA). From the model outputs, we diagnose a closed

10   form of the water mass budget for AABW that explicitly accounts for transport across the WG boundary, surface forcing, interior mixing, and numerical mixing. We examine the annual mean climatology of the WMT budget terms, the seasonal climatology, and finally the interannual variability. Our finding suggests that the relatively coarse resolution of these models did not realistically capture AABW formation, export and variability. In ECCO and SOSE, we see strong interannual variability in AABW volume budget. In SOSE, we find an accelerating loss of AABW during 2005-2010, driven largely by interior

15   mixing and changes in surface salt fluxes. ECCO shows a similar trend during a 4-yr time period starting in late 2007, but also reveals such trends to be part of interannual variability over a much longer time period. Overall, ECCO provides the most useful timeseries for understanding the processes and mechanisms that drive WMT and export variability in the WG. SODA, in contrast, displays unphysically large variability in AABW volume, which we attribute to its data assimilation scheme. We also examine correlations between the WMT budgets and large-scale climate indices, including ENSO and SAM, and find no strong

20   relationships.

1 Introduction

Antarctic Bottom Water (AABW) formation plays a key role in the climate system as it provides a pathway for ventilation of abyssal waters, transport of nutrients and tracers (i.e. nitrogen, phosphorous and oxygen), and storage for large amounts of carbon (Ito et al., 2015). It is the coldest and densest water mass in the global ocean, and comprises about 36 % of the global deep ocean volume (Johnson, 2008; Purkey and Johnson, 2013; Purkey et al., 2018). AABW is a key player to the abyssal cell of the Meridional Overturning Circulation (MOC), an essential component of the ocean circulation that has important global effects on the Earth's climate system. The MOC is responsible for transporting and redistributing heat, salt, carbon and nutrients (Talley, 2013). The abyssal cell circulation of the MOC is dependent upon surface forcing and interior mixing (Nikurashin and Vallis, 2011, 2012). Turbulent mixing sets the depth to which AABW upwells, and provides a mechanism for waters to transform into AABW and circulate into the abyssal ocean (Nikurashin and Vallis, 2011, 2012; Ferrari et al., 2014; Nycander et al., 2015). The abyssal cell is ventilated through coastal polynyas and plumes of dense, high-oxygen-containing cold waters cascading down the continental boundaries (Williams, 2001).

Serving as the primary production site (supplying 40-50 %, Stewart (2021)) of AABW, and as a major carbon sink (Brown et al., 2015), is the Weddell Gyre (WG). It is the most prominent gyre in the Southern Ocean and is pivotal for the MOC and for ventilating the ocean. The WG is a clockwise-flowing subpolar gyre east of the Antarctic Peninsula, driven by the wind stress curl in this region (Vernet et al., 2019). In the WG, relatively warmer deep waters from the north bring in heat; as these waters upwell they are cooled and freshened, transforming into surface water masses that become part of the sources for bottom water formation (Gordon et al., 2020).

Recent mooring data in the Weddell suggest significant seasonal and interannual variability of AABW properties exiting the WG (Gordon et al., 2020). It is hypothesized that these variabilities are linked to the coupling of large-scale climate forcings, the El Niño Southern Oscillation and the Southern Annular Mode (SAM), through wind stress variability that leads to the variability in the WG strength and its density structure (Gordon et al., 2007; Meredith et al., 2008; Gordon et al., 2010; McKee et al., 2011; Armitage et al., 2018; Gordon et al., 2020). However, the specific thermodynamic mechanisms that link variability in surface forcings to AABW export remain unclear.

A crucial concept to understanding AABW formation variability, and ultimately the variability of the MOC, is water mass transformation (WMT). A water mass is defined as the water bounded by isosurfaces of a tracer. Any tracer can be used, but the most common tracers for WMT analysis are temperature, salinity, and potential density. The transformation of a water mass occurs when the water mass' density is altered through irreversible thermodynamic processes. In order for the MOC to exist, water masses must change density classes as they circulate between the surface and abyss, just like North Atlantic Deep Water (NADW) and AABW. The next section provides an overview of the WMT theory and explains its value in providing insight to global ocean circulation.

While mooring observations such as described in Gordon et al. (2020) are useful for characterizing observed variability in water masses, they cannot provide a closed water mass budget, which requires dense observations of dynamic and thermodynamic fluxes in space and time. So in order to investigate the dynamics and thermodynamics of temporal variability in AABW using

the WMT framework, we turn to three state-of-the-art, data-assimilating ocean reanalysis products. Such products are a useful tool in studying regions, such as the WG, that lack consistent and comprehensive observations, and for investigating physical mechanisms that drive variability. While reanalyses are far from perfect representations of the ocean state, they represent the best attempt to synthesize diverse observations in a consistent way. Even if physical processes such as coastal polynyas are not always represented accurately in ocean reanalyses (Mazloff et al., 2010), there is still value in understanding their internal dynamic and thermodynamic budgets. By diagnosing WMT in these reanalyses, we can probe the relationships between ocean surface fluxes with a changing climate, how climate variability influences sea ice expansion and water mass transformation rates, and how that ultimately affects the abyssal water properties and circulation of the lower MOC cell. Understanding how the deep ocean reacts to a warming climate will give us insight to how oceans will contribute to sea level rise and CO_2 content in the atmosphere. Purkey and Johnson (2010) have shown that the 80% radiative imbalance in the atmosphere that have gone into heating the ocean has lead to a global change in abyssal heat content equivalent to adding 10% to the total ocean heat storage, increasing rates of steric sea level rise by 8%. The global impacts of the AABW circulation system on biological productivity and carbon and heat uptake, particularly in the context of climate change, makes AABW variability in the WG worth studying extensively (Vernet et al., 2019). With datasets as described in section 3, and the water mass transformation (WMT) framework outlined by Walin (1982) (Sect 2), we strive to provide insight into the mechanisms and drivers of MOC variability in the WG. Our study does not attempt to provide an authoritative timeseries of the "true" WMT and overturning variability in the WG; as the analysis shows, these three models show very different behavior. Our focus is on methods and mechanisms.

Our paper is organized as follows: In Section 2, the theory of WMT is introduced and we detail how the WMT budget was calculated. In Section 3 we talk about the observational and model data used. Observational data from the World Ocean Atlas was used to compare to modelled bottom temperatures and salinities. The average, climatological and interannual variability of volume tendency, transport and transformation is discussed in Sections 4.1, 4.2, 5, respectively. Finally, the findings from the Section 5 is discussed and compared with similar studies in Section 6.

2   Water Mass Transformation Theory

Here we provide a brief introduction to the WMT framework, first employed by Walin (1982). The WMT-framework, in this context, allows for the separation of explicit mechanical and thermodynamic processes on ocean circulation (Walin, 1982; Groeskamp et al., 2016, 2019) due to surface fluxes, advective transport, and diffusive mixing.

A water mass is defined as the water bounded by isosurfaces of a tracer. Any tracer can be used, but the most common tracers for WMT analysis are temperature, salinity, and potential density. Here we use σ_2 - potential density referenced to 2000 dbar - because of its ability to characterize stratification through the deep and abyssal ocean. AABW in the WG region typically exists below 2000 m. σ_2 was computed using the Jackett and Mcdougall (1995) ocean equation of state. (For notational simplicity, henceforth we will write σ instead of σ_2.) The limitation of investigating WMT through potential density is the inability to quantify the effect of cabbeling and thermobaricity on WMT, potential misrepresentation of neutral mixing (Iudicone et al., 2008b), and inability to distinguish water masses of the same density but different temperature / salinity (Evans et al., 2018).

Here we define transformation of a water mass as the change in density of the fluid parcel due to its change in heat and salt content. Computing the transformation budget for a basin or a remote region, such as the Weddell, can further our understanding by providing quantitative insight into the drivers of water mass variability.

The potential density σ of seawater evolves according to:

$$\frac{D\sigma}{Dt} = \dot{\sigma} = \frac{\partial \sigma}{\partial \theta}\dot{\theta} + \frac{\partial \sigma}{\partial S}\dot{S} \tag{1}$$

where the factors $\frac{\partial \sigma}{\partial \theta}$ and $\frac{\partial \sigma}{\partial S}$ are the thermal expansion and haline contraction coefficients, respectively. This expression includes both a thermal component:

$$\frac{D\theta}{Dt} = \dot{\theta} = G^{\theta}_{hdiff} + G^{\theta}_{vdiff} + G^{\theta}_{surf} + G^{\theta}_{sw} \tag{2}$$

where G^{θ}_{hdiff} represents the temperature tendency due to horizontal/isopycnal mixing, G^{θ}_{vdiff} is the tendency due to vertical/diapycnal mixing, G^{θ}_{surf} is the surface forcing, and G^{θ}_{sw} is the shortwave penetration; and a haline component

$$\frac{DS}{Dt} = \dot{S} = G^{S}_{hdiff} + G^{S}_{vdiff} + G^{S}_{surf} \tag{3}$$

where the terms represent the salinity tendency due to the same non-conservative terms as for temperature, except for shortwave radiation term. We use these forms of the heat and salt budget because they correspond to how those budgets are diagnosed from numerical simulations.

To understand the equations to come, briefly we cover the Heaviside and delta functions. The Heaviside function, $\mathcal{H}$, is 0 when the argument is negative, and 1 for positive arguments. The Heaviside function is the integral of the delta function where

$$\frac{\partial \mathcal{H}(x)}{\partial x} = \delta(x) \tag{4}$$

This approach allows us to define a region under a reference isopycnal ($\tilde{\sigma}$). The density field is a function of x, y, z and time, meaning

$$\sigma = \sigma(x,y,z,t). \tag{5}$$

so that the total volume of water *denser* than $\tilde{\sigma}$ within a region R is given by

$$\mathcal{V}(\tilde{\sigma},t) = \int_{R} \mathcal{H}(\tilde{\sigma} - \sigma)dV \tag{6}$$

i.e. the cumulative volume distribution.

The WMT budget for region R in the following equation, expresses the relationship between the time evolution $\mathcal{V}$ to the inflow/outflow transports (Ψ) on the basin boundary, plus the thermodynamic transformation (Ω) occurring in the basin interior:

$$\frac{\partial \mathcal{V}}{\partial t} = \Psi + \Omega, \tag{7}$$

where

$$\Psi(\tilde{\sigma}, t) = -\int_{\delta R} (\mathbf{u} \cdot \hat{\mathbf{n}}) \mathcal{H}(\tilde{\sigma} - \sigma) dA \tag{8}$$

(δR is the region boundary and $\hat{\mathbf{n}}$ is the unit normal on the boundary) and

$$\Omega(\tilde{\sigma}, t) = -\int_{R} \delta(\tilde{\sigma} - \sigma)\dot{\sigma} dV. \tag{9}$$

The $\dot{\sigma}$ in Eq. (9) comes from the potential density conservation equation (Eq. (1)). It represents the sum of the temperature and salinity components (Eqs. (2) and (3), respectively) of the non-conservative tendencies from horizontal and vertical diffusion, surface forcing and shortwave penetration (potential temperature only) (Abernathey et al. (2016), Supplemental Information). The WMT framework helps us discern the contributions to the water mass variability by quantitatively relating it to the driving processes of surfacing forcing and advective transport to interior mixing.

2.1 Numerical Implementation

In order to assess the mechanisms behind AABW transformation and circulation variability, a fully closed WMT budget is desirable. To calculate this, we must first close the temperature and salinity budgets. WMT volume budget analysis was conducted using ECCO, SOSE, and SODA reanalysis data. In all of these cases, the ocean is divided into discrete layers $\tilde{\sigma}_n$, and each of the relevant terms is calculated inside these discrete layers. The discrete analog of the cumulative volume integral (6) is

$$\mathcal{V}(\tilde{\sigma}_n, t) = \sum_{i,j,j} \Delta V \mathcal{H}(\tilde{\sigma}_n - \sigma) \tag{10}$$

where the summation is over each model grid cell within the region of interest and ΔV is the finite volume of each cell. Henceforth we use the shorthand $\mathcal{V} = \text{cumsum}_\sigma(\Delta V)$ to denote this operation.

The time-rate of volume change was computed and balanced by the calculated σ total tendency ($\Omega_{tottend}$) and a residual (R1) due to discretization of isopycnal layers:

$$\frac{\partial \mathcal{V}}{\partial t} = \Omega_{tottend} + R1 \tag{11}$$

where

$$\Omega_{tottend} = -\frac{\partial}{\partial\tilde{\sigma}}\text{cumsum}_\sigma(G^\sigma_{tottend}) \,, \tag{12}$$

and where $G^\sigma_{tottend} = (\partial\sigma/\partial\theta)G^\theta_{tottend} + (\partial\sigma/\partial S)G^S_{tottend}$ is the model's total tendency for potential density, a weighted sum of total tendencies for temperature and salinity. This term is the sum of conservative tendencies due to horizontal and vertical advection, non-conservative tendencies due to horizontal and vertical diffusion, and surface forcings (including shortwave penetration for the potential temperature component). It is helpful to calculate R1 explicitly in order to determine if the chosen σ bin size is appropriate. We found that the budgets were not sensitive to changing σ bin sizes. Smaller bin sizes meant higher resolution; however that did not significantly change R1 and increased computational costs.

Next, the total advection tendency term (Ψ_{adv}) is decomposed to σ's velocity component (Ψ_{vel}) and a residual term (R2) attributed by a yet-to-be-determined combination of numerical mixing and numerical cabbeling effects:

$$\Psi_{adv} = \Psi_{vel} + R2 \tag{13}$$

The term

$$\Psi_{adv} = -\frac{\partial}{\partial\tilde{\sigma}}\text{cumsum}_\sigma(\frac{\partial\sigma}{\partial\theta}G^\theta_{adv} + \frac{\partial\sigma}{\partial S}G^S_{adv}) \tag{14}$$

represents the direct effect, as output from the models, of advection of temperature and salinity on the total tendency of potential density in each grid cell, while

$$\Psi_{vel} = -\text{cumsum}_\sigma(\mathbf{u}\cdot\hat{\mathbf{n}}\delta A). \tag{15}$$

is the net transport across the region boundary, accumulated in $\tilde{\sigma}_n$ bins; this is the conventional overturning streamfunction. In the continuous world, Ψ_{adv} and Ψ_{vel} can be shown to be mathematically identical. However, numerical discretization of the advection operator yields a residual term representing non-advective affects of the advection scheme. This residual has in fact been used to quantify numerical mixing in other studies (Holmes et al., 2021). Separating out the numerical residual allows us to explicitly see the volume-transport of certain densities by purely physical inflow/outflow mechanisms, and by a mixing term.

Water mass transformation, Ω_{tf}, was computed by summing the rest of the tendency terms due to non-conservative, thermodynamic processes such as diffusion, shortwave radiation and surface forcings of heat and freshwater:

$$\Omega_{tf} = -\frac{\partial}{\partial\tilde{\sigma}}\text{cumsum}_\sigma\left[\frac{\partial\sigma}{\partial\theta}(G^\theta_{hdiff} + G^\theta_{vdiff} + G^\theta_{surf} + G^\theta_{sw}) + \frac{\partial\sigma}{\partial S}(G^S_{hdiff} + G^S_{vdiff} + G^S_{surf})\right] \tag{16}$$

By defining residuals in this way, we arrive at a numerical form of eq. 7 below which is closed by construction:

$$\frac{\partial\mathcal{V}}{\partial t} = \Psi_{vel} + R2 + \Omega_{tf} + R1. \tag{17}$$

160   Since R2 represents numerical mixing, we can more concisely write equation 17 to be

$$\frac{\partial \mathcal{V}}{\partial t} = \Psi_{vel} + \Omega^* + R1,$$ (18)

where

$$\Omega^* = \Omega_{tf} + R2.$$ (19)

       We can even further decompose the various G_{surf} terms by breaking them into different sub-components. One such analysis

165   we do here is to separate G_{surf}^{S} into a component directly related to sea ice and a component due to direct exchange of freshwater

       with the atmosphere and land, as done also by Abernathey et al. (2016). We found minimal contribution of E-P-R to surface salt

       fluxes, and a dominant role from sea ice activity. Specifically, we saw brine rejection activity throughout most of the season

       until summer when there were spikes in ice melt during a few summer months (amplitude usually matching the highest brine

       rejection spike). SODA does not provide any tendency diagnostics; however, it does provide the velocity field. Thus, in SODA

170   we simply define Ω^* via the residual: $\Omega^* = \partial \mathcal{V}/\partial t - \Psi_{vel}$.

       Equation (17) represents the WMT volume budget expressed by explicit terms due to physical and thermodynamic processes

       captured by the model. Now we can see the time-rate of volume change is balanced by the physical transport into and out-of the

       WG, plus the residual mixing term, the transformation term, and numerical discretization residual. Subsequent plots in sections

       4.1, 4.2 and 5 display each term's contribution to the total WMT volume budget.

175   3   Data & Models

The observational data and numerical simulations used in this project are described here. The strengths and limitations of the

models are mentioned in each section, and evaluation of each numerical model is discussed in section 3.5.

3.1   World Ocean Atlas

We used observational temperature and salinity as a baseline for validating the use of each model. Evaluation of each model

180   compared with observations is in Sect. 3.5. The observational temperature and salinity data are from the World Ocean Atlas

       2013 (WOA) (Locarnini et al., 2013; Zweng et al., 2013; Levitus et al., 2014). WOA is a set of objectively analyzed 1° gridded

       climatological fields of in situ temperature and salinity. The 1° climatological fields averaged over 2005-2012 are presented in

       this paper as a means for model validation assessment.

       Temperature and salinity profile data were obtained from bottled samples; ship-deployed Conductivity-Temperature-Depth

185   (CTD); Mechanical, Digital and Expendable Bathythermographs (XBT), profiling floats, moored and drifting buoys, gliders,

       undulating oceanographic recorder (UOR), and pinniped mounted CTD sensors. WOA contains both observed levels profile

       data and standard depth profile data with various quality control flags applied. In most regions with sparse data coverage, such

as the WG region, flagged data seen as outliers were not removed because they may still represent legitimate values; and are therefore, included in the climatological periods used here (Locarnini et al., 2013; Zweng et al., 2013; Levitus et al., 2014).

3.2 Estimating the Circulation and Climate of the Ocean (ECCO)

The Estimating the Circulation and Climate of the Ocean version 4 release 3 (ECCO) state estimate is a reconstruction of the 3-D time-varying ocean and sea ice state (Forget et al., 2015). Produced from MITgcm, ECCO has approximately 1° horizontal grid resolution and 50 vertical levels of varying thickness. It provides monthly-averaged 3-D ocean, sea-ice, and air-sea flux fields; 2-D daily-averaged ocean and sea-ice fields, and 6-hourly atmosphere fields, all covering the period Jan 1, 1992 to Dec 31, 2015. The ECCO state estimate provides a statistical best fit to observational data; however, unlike other ocean reanalyses that directly adjust the model state to fit the data, such as the Simple Ocean Data Assimilating model described in section 3.4, ECCO is a free-running model that simulates what is observed in the ocean based on the governing equations of motions, a set of initial conditions, parameters, and atmospheric boundary conditions. Some observational data ECCO uses are from Argo floats, shipboard CTD and XBT measurements, marine mammals, mooring data, Radar Altimeter Database System, satellite products from National Snow and Ice Data Center(NSIDC) and programs such as SSM/I DMSP-F11 and -F13, and SSMIS DMSP-F17 (Fukumori et al., 2018).

The ECCO state estimate satisfies physical conservation laws, with no unidentified sources of heat and buoyancy. Due to the model's dynamically consistent nature, it conserves heat, salt, volume, and momentum (Wunsch and Heimbach, 2007, 2013); and the state estimate can be used to explore the origins of ocean heat, salt, mass, sea-ice, and regional sea level variability (Forget et al., 2015). It uses a non-linear free surface combined with real freshwater flux forcing and the scaled height coordinate; and users of ECCO are able to assess model-data misfits (Forget et al., 2015). Known issues of the state estimate are mentioned for the first release in (Forget et al., 2015). For example, ECCO has residual systematic errors, especially in regions with sparse data (Buckley et al., 2017).

3.3 Southern Ocean State Estimate

The Southern Ocean State Estimate (SOSE) is a model-generated best fit for Southern Ocean observations (Mazloff et al., 2010). It is a solution to the MITgcm, constructed in spherical coordinates with 42 vertical levels of varying depth (m), and a C-gridded dataset at 1/6° horizontal resolution, available at timestamps daily and annually (Mazloff, 2008). Its iteration runs at 5-day averages starting from Jan 1-5 2005, ending Dec 31 2010.

SOSE is also a data-assimilating model. It uses similar observation data as ECCO. Observations of daily sea ice concentration have been attained from the NSIDC. Some limitations are similar to that of reanalyses in regards of regions and variables being more reliable with more observations covered in those areas, and the opposite being true for regions with sparse data. SOSE provides a self-consistent state estimate that satisfies momentum, volume, heat and freshwater conservation. Some of its key strengths are that SOSE has a better spatial and temporal resolution than most state estimate models and is the highest-resolution model used in this study. It is dynamically consistent and best-fit to available 190 observations, and its biases are well-documented (Mazloff and National Center for Atmospheric Research Staff, 2021).

This study examines the Weddell Sea region, and so far one major bias has been found during our analysis: SOSE produces an open-ocean polynya in the first year of its run (2005) which was not observed in the real ocean; therefore, this year is removed from the time-mean and climatology, but the anomalous interannual variability still includes the year 2005.

3.4 Simple Ocean Data Assimilation

225 The Simple Ocean Data Assimilation ocean/sea ice reanalysis (SODA) is the third numerical model used for our water mass transformation analysis. The SODA3 reanalyses are built on the Modular Ocean Model, version 5, ocean component of the Geophysical Fluid Dynamics Laboratory CM2.5 coupled model (Delworth et al., 2012), with fully interactive sea ice on a $0.25° \times 0.25°$ horizontal and 50-level vertical resolution (Carton et al., 2018). The sea ice data is taken from the Geophysical Fluid Dynamics Lab's Sea Ice Simulator model (Delworth et al., 2012). It does not include flow of ice from continental regions

230 into the ocean, including ice shelves and their interaction with the ocean. Improvements have been made in SODA3 such as upgrades to the SST datasets and a 40 % increase in hydrographic data from the latest release of the World Ocean Database. Earlier generations of ocean reanalysis have contained systematic errors that have several sources, including measurement bias, inaccurate model physics and numerical resolution, and biases in fluxes and initial conditions. The release of SODA3 was an effort to address these broad issues; for example, the adoption of the iterative flux correction procedure of Carton et al. (2018)

235 addresses the bias in surface forcing in which flux error is estimated from the misfits obtained from an initial ocean reanalysis to alter fluxes for a revised ocean reanalysis. SODA3 was also upgraded to be an ensemble reanalysis, for which the ensemble spread provides an estimate of uncertainty. A comparison to ORAS5 and ECCOv4r3 is provided in (Carton et al., 2019).

SODA3 is included with finer eddy-permitting spatial resolution, active sea ice, and bias adjustment. The version this study uses is SODA3.4.2 (SODA henceforth), which means that the assimilated data is restricted to the basic hydrographic data and

240 SST with meteorological forcing derived from the European Centre for Medium-Range Weather Forecasts interim reanalysis (ERA-Interim) daily average surface radiative and state variables (Dee et al., 2011) and the COARE4 bulk formula with flux bias correction applied. The ocean and ice data runs every 5 days running through Jan 4, 1993 to Dec 19, 2019, and the transport files every 10 days from Jan 7, 1993 to Dec 17, 2019. There were jumps in the salt field from the ocean files occurring before 1997 that we suspect is the result of the reanalysis's nudging technique. For this reason, we have used SODA running from

245 February 15, 1997 to Dec 17, 2019.

The biggest difference between SODA and ECCO and SOSE is their method of data assimilation. ECCO and SOSE use the adjoint data assimilation method which optimizes the initial conditions and model parameters by incorporating observation data to a physics-based numerical simulation. The SODA experiment uses an optimal interpolation method for their data assimilation in which the ocean state is constructed from a forecast using a linear deterministic sequential filter and based on the difference

250 between observations and the forecast mapped onto the observation variable and its location (Carton et al., 2018). Due to the method of data assimilation, it is not possible to diagnose a closed heat budget in SODA, and therefore we cannot explicitly calculate Ω. However, we can calculate $\partial V/\partial t$ and Ψ. So in the following analysis, we infer Ω as a residual.

3.5 Model Assessment

It is well known that numerical models struggle to capture the complex physics on the Antarctic shelves that determine AABW properties and circulation (Heuzé et al., 2013). Although these models assimilate data, they are still constrained by their resolution and physical parameterizations. In this section we assess each model against the World Ocean Atlas data. This step gives a base for assessing each model's reliability in simulating ocean physics in a region with limited observational data, such as the Weddell Sea region. Such validation was assessed by comparing bottom temperature and salinity spatial distributions, as well as time-averaged Temperature-Salinity (TS) distributions, in the WG region between ECCO/SOSE/SODA and WOA. ECCO and SODA were averaged over the same time period as the WOA product (2005-2012); except for SOSE, whose time period only spans 2005-2010. Noting that the time period between SOSE and observation are different, we still execute the comparison with what is available; but recognize that this introduces unknown biases in our comparison. The boundaries of the WG region are defined here to be from 65 °W to 30 °E, and from 78 °S to 57 °S (Gordon et al., 2007; Neme et al., 2021).

Figure 1 (a), (c), (f) and (i) shows the time-mean bottom temperatures in the WG region for WOA (2005-2012), ECCO (2005-2012), SOSE (2006-2010) and SODA (2005-2012), respectively. The coldest temperatures in each model are located near the coast of Antarctica and gradually becomes warmer equatorward, with signatures of the Antarctic Circumpolar Current (ACC) present in the upper left. However, in ECCO there appears to be a strip of relatively warmer water enclosing the coldest temperatures before the more gradual equatorward warming is displayed. Showing the temporal standard deviation of temperature, which we use as a proxy for the (unknown) reanalyses uncertainties, in Fig. 1 (d), (g) and (j) from ECCO, SOSE and SODA, respectively, we can see that in ECCO and SODA (Fig. 1 (d) and (j)) there is little spatial variability in bottom temperature; whereas in SOSE (Fig. 1 (g)), there is a lot of variability in the open region of the Weddell. Furthermore, looking at the difference in temperature between each model and WOA (Fig. 1 (e), (h) and (k)), we also see that ECCO and SODA are overall warmer than observations (Fig. 1 (e) and (k)). From ECCO and SODA, the difference is as high as 2° C; however, in SODA, the model on average simulates colder bottom temperatures along the Antarctic Peninsula (Fig. 1 (k)). In SOSE, however, there is less of a difference between simulated and observed temperature (Fig. 1 (h)). The region with hash marks denotes the places where the difference between modelled and observed temperatures is less than the standard error of the observational estimates; and as we can see in SOSE (Fig. 1 (h)), the model's bottom temperature agrees with WOA in the open ocean.
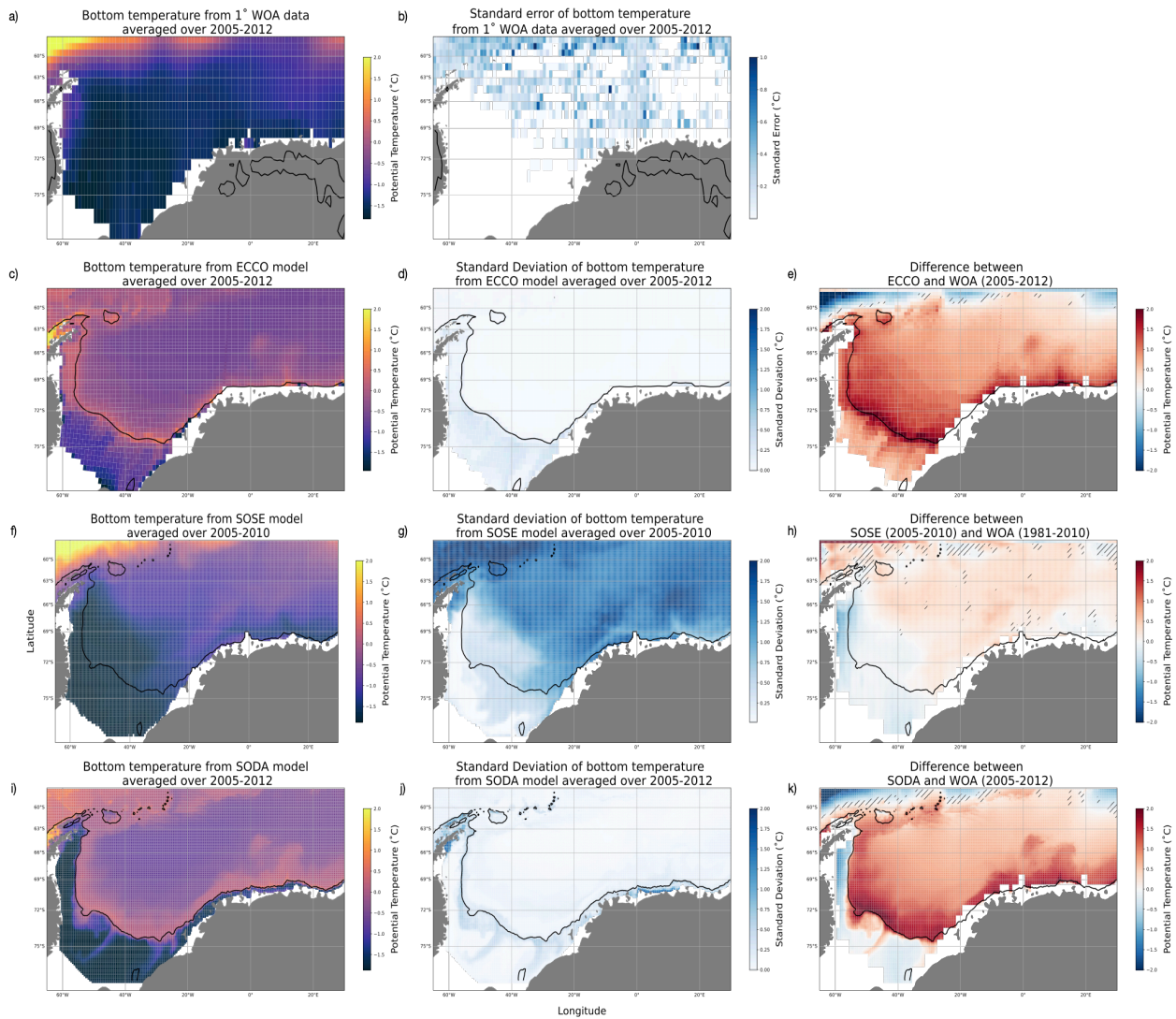
Figure 1. Annual mean of bottom temperatures (°C) of the Weddell Gyre region for (a) WOA (2005-2012), (c) ECCO (2005-2012), (f) SOSE (2005-2010) and (i) SODA (2005-2012). Standard error of WOA observations is shown in (b); and temporal standard deviations are shown for (d) ECCO, (g) SOSE and (j) SODA. The differences between the observed and simulated bottom temperatures are shown in (e) ECCO, (h) SOSE and (k) SODA. The black hash lines denote the areas where the difference between model and WOA is less than the observation's standard error. The black contour represents the 1000 m isobath.

Following a similar assessment for bottom salinity, the spatial distribution of salinity in all three models and WOA appears to be more uniform than their respective temperature fields. The distribution in SOSE, Fig. 2 (f), indicates that the model is on

280 average fresher than the others. Another distinction that stands out is the more variable spatial distribution in ECCO and SODA's salinity field (Fig. 2 (c) and (i), respectively), with fresher water located closest to the coast of the continent. In ECCO, however, there are saltier plumes around 40 °W (Fig. 2 (c)), just north of where the Filchner-Ronne Ice Shelf would be, indicating that ECCO is reproducing High Salinity Shelf Water (HSSW) in around the same areas present in the observational data (Fig. 2 (a)). Looking at the temporal deviations, we see in ECCO and SODA little variability overall in bottom salinity (Fig. 2 (d) and (j)). In

285 SODA, however, there is a significant sliver of variability in the eastern part of the region along the coast. In SOSE (Fig. 2 (g)), there are strong temporal deviations from the average salinity field along the coast of the Peninsula. In Fig. 2 (e) and (k), there is very little difference between model and observational bottom salinity, as is indicated by the black hash marks. The biggest difference we see between model and observed salinity is between SOSE and WOA. As we saw from Fig. 2 (f), SOSE is much fresher than what is observed and simulated in the other models, by about 0.5 psu.
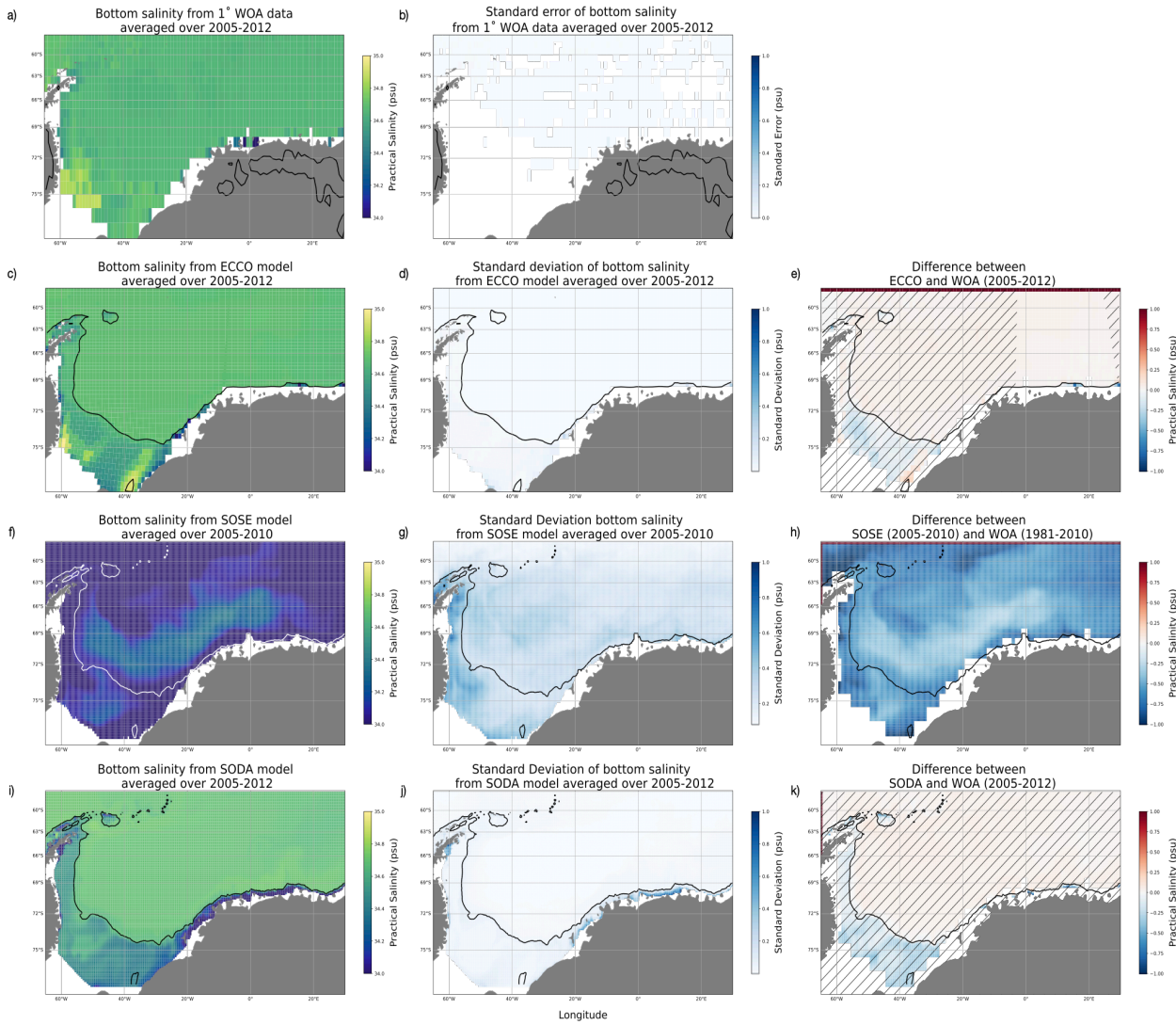
Figure 2. Annual mean of bottom salinity (psu) of the Weddell Gyre region for (a) WOA (2005-2012), (c) ECCO (2005-2012), (f) SOSE (2005-2010) and (i) SODA (2005-2012). Standard error of WOA observations is shown in (b); and temporal standard deviations are shown for (d) ECCO, (g) SOSE and (j) SODA. The differences between the observed and simulated bottom salinities are shown in (e) ECCO, (h) SOSE and (k) SODA. The black hash lines denote the areas where the difference between model and WOA is less than the observation's standard error. The black contour represents the 1000 m isobath.

290   To further test the validity of model representation of real world processes, volume-weighted TS distributions were compared

between model and observations (Fig. 3). Once again, ECCO and SODA were averaged over the same climatological period

as WOA (2005-2012); and SOSE was averaged over 2005-2010. The difference between each model's TS distribution and

observation is shown in Fig. 4. The approximate temperature and salinity profile ranges of AABW are as follows: -0.2° C $< \theta <$

-0.7° C and 34.6 psu $<$ S $<$ 34.7 psu (Carmack, 1974; Mackensen et al., 1996); and is delineated by the cyan box in both figures.

295   Looking at Fig. 3, an obvious observation is that all three models' TS distribution have a similar shape and have more spread

over the lighter density ranges than in WOA. WOA's spread across density contour 1037.0 kg m^{-3} and lighter, however, is

unlike any of the models' TS distribution. Observation and models display that the most voluminous waters in the WG are

Circumpolar Deep Water (CDW) and AABW since their densities and temperature-salinity ranges exist in those regions (darkest

blue). One notable feature of Fig. 3 is the strong peak in the SODA TS histogram around T = 0. This feature does not appear in

300   the hydrography or the other models. We investigated the peak extensively, by isolating the values close to zero and plotting the

geography and spatial variability. There was no apparent pattern to these values which we could discern; they are a real feature

of the SODA temperature output.

We took the difference between each model's and observed TS distribution and viewed the difference on a semi-logarithmic

scale, Fig. 4. This allows us to see a wider range of data. All models underrepresent the coldest, densest HSSW in TS space.

305   This suggests biases in the AABW formation processes. In the CDW range, we observe that the models generally have a more

spread-out TS distribution, in contrast to WOA where CDW has a tighter relationship. We speculate that this bias may be related

to a misrepresentation of interior mixing processes.

TS Diagrams
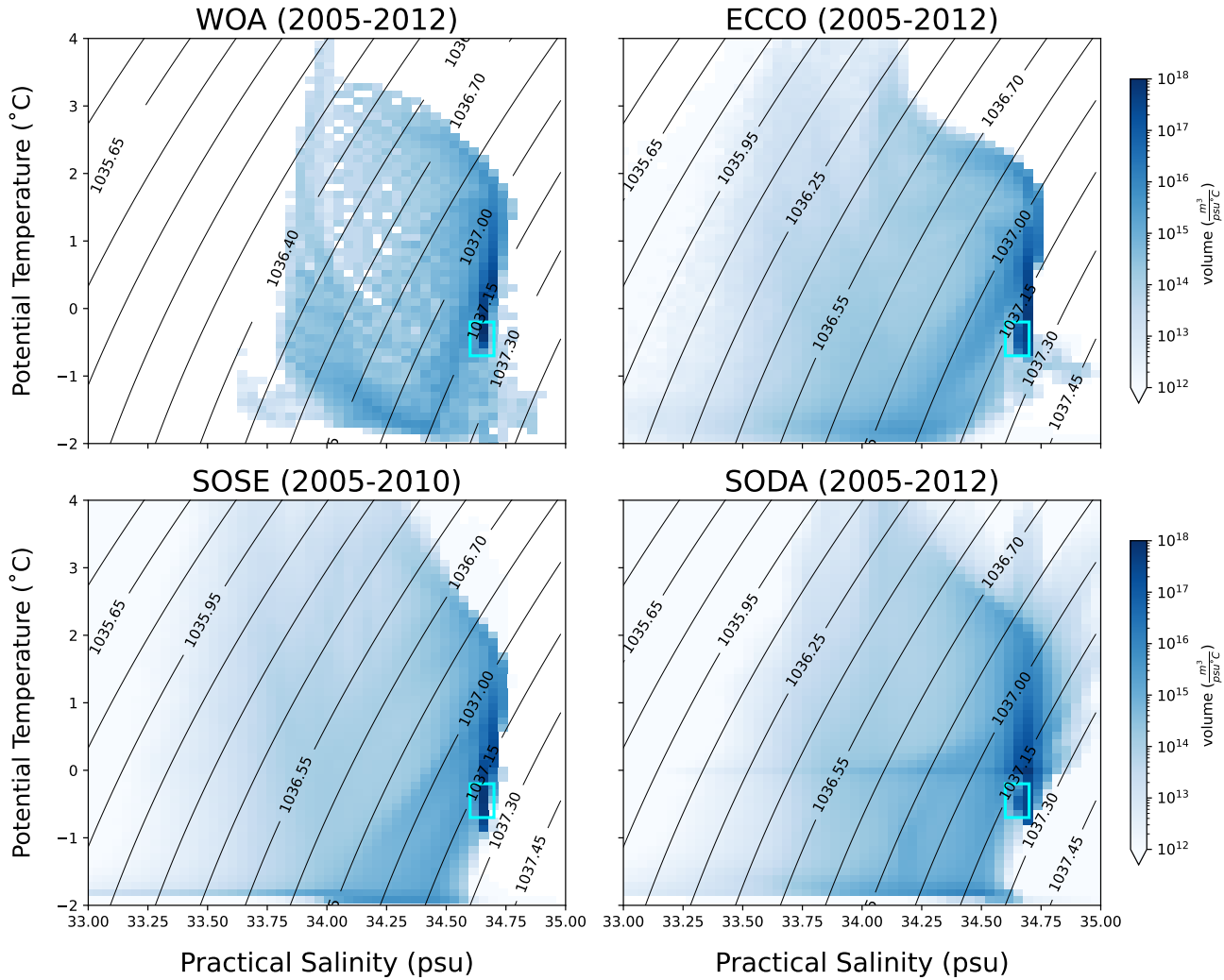
Figure 3. Averaged temperature-salinity distribution of the WG region for WOA, ECCO, SODA (2005-2012) and SOSE (2005-2010). Contour lines represent potential density referenced at 2000 m (σ_2). The cyan box shows the temperate-salinity range of AABW.
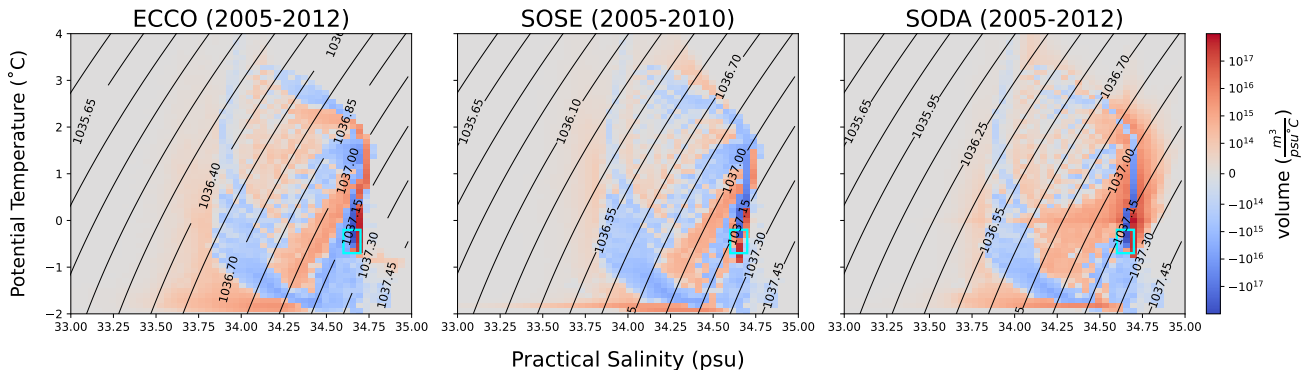
Figure 4. Averaged temperature-salinity distribution of the difference between WOA and each model. Contour lines represent potential density referenced at 2000 m (σ_2). The cyan box shows the temperate-salinity range of AABW.

Overall, ECCO and SODA appear to reproduce bottom salinity where the difference between modeled and observed values is less than the observation's standard error (as denoted by the hash marks). SOSE reproduces bottom temperature with the difference less than WOA's standard error as well. Simulated bottom temperature in ECCO and SODA, however, is warmer than what is observed; and SOSE has a fresher tendency than what is observed. These are important biases in each model to note as we continue our analysis of AABW variability using all three models.

4   Climatological WMT Budgets

4.1   Annual Mean

We first examine the annual-mean WMT budget, which represents the long-term mean transformation and overturning structure of the WG, averaging over all spatial and temporal variability. Figure 5 (a), (b) and (c) shows the annual mean budget from ECCO, SOSE and SODA, respectively. The black line represents the time evolution of the cumulative water mass volume distribution, $\partial V/\partial t$, in the WG region during each model's respective time period. It is balanced by the total inflow/outflow transports (Ψ, red line) and mean transformation (Ω^*, purple line), which includes the residual due to numerical mixing. Conceptual models usually assume that the system is in a steady state balance between overturning and transformation ($\partial V/\partial t = 0$), but that is clearly not the case for any of the models examined here. The existence of a tendency indicates a model drift and / or low-frequency variability over the climatological period.

In σ_2 coordinates the water masses that are the Weddell's recipe for AABW are distinguished by their densities as follows: CDW/WDW ($1037.13 < \sigma_2 < 1037.24 \, \mathrm{kg \, m^{-3}}$) and WSBW/HSSW/ISW ($\sigma_2 \geq 1037.2 \, \mathrm{kg \, m^{-3}}$). Our budget coarsely separates all water into two classes which are delineated by a boundary, $\sigma^\dagger$: bottom water (denser than $\sigma^\dagger$) and deep water (by volume, mostly CDW and its regional variants). Due to volume conservation, in this construction, the transport of bottom water across

the basin boundary is equal and opposite to the transport of deep water. The dividing isopycnal $\sigma^\dagger$ is defined for each model via the minimum of the overturning streamfunction (Ψ). Because the streamfunction is a cumulative integral quantity, the framework defines AABW transport as the flow across the boundary of all water denser than $\sigma^\dagger$. So one single transport value represents
330   both the deep outflow and the equal-and-opposite bottom water inflow. Recapitulating, here we define AABW's density ($\sigma^\dagger$) specific to each model based on where each Ψ reaches its extreme (minimum value) after crossing zero. The values of $\sigma^\dagger$ are 1037.155 kg m^{-3} for ECCO, 1037.145 kg m^{-3} for SOSE, and 1037.175 kg m^{-3} for SODA. On average, as shown by the negative extremum of Ψ, AABW is exported from the region at the rate of 7.9 Sv in ECCO, 4.9 Sv in SOSE, and 1.9 Sv in SODA. The export is countered by thermodynamic transformation (Ω) by 3.6 Sv in ECCO and 0.4 Sv in SODA, and paired by
335   Ω in SOSE by 1 Sv. This leads to a total volume loss of the bottom water class of 2.8 Sv in ECCO, 6.6 Sv in SOSE and 1.5 Sv in SODA. The export value from ECCO is similar to the mean outflow value of Kerr et al. (2012) who found mean outflow of AABW using a 1/12° 20-yr global ocean simulation to be 10.6 ± 3.1 Sv. We note that though Kerr et al. (2012) obtained this value from a transect at the tip of the Antarctic Peninsula, they do attempt to capture the dominant outflow of the Weddell sea AABW. Similar transport value of AABW have been reported by Talley et al. (2003), who determined 8.5Sv of AABW
340   traveling northward in the Atlantic sector of the Southern Ocean meridional overturning circulation.

We now examine the thermodynamic processes driving transformation in more detail. AABW transformation in ECCO (Fig. 6 (a)) is mainly due to brine rejection at the surface (orange dashed line). We categorize the transformation from surface salt fluxes as influence only from sea ice since our analysis showed an almost negligible role from the atmosphere. Therefore, positive transformation values are associated with brine rejection, and negative values with ice melt. The effects of surface cooling
345   and mixing are generally confined to lighter water masses in the region and tend to cancel each other out. However, mixing does have a stronger tendency to lighten bottom water (by about 4.5 Sv) than surface cooling induced positive transformation (0.6 Sv). In ECCO, the dominant impact of brine rejection on transformation (7.4 Sv) is similar to Iudicone et al. (2008a) who found brine rejection dominating transformation of bottom water by ∼5 Sv. In SOSE (Fig. 6 (b)) the effect of transformation on bottom water behaves opposite to ECCO. SOSE's Ω is driven by mixing (2.8 Sv) and is countered by an equal combination of
350   surface cooling and brine rejection (both 0.9 Sv). Overall, the ECCO and SOSE models are in qualitative agreement with the literature of what is known about bottom water circulation in the Weddell Sea (Carmack and Foster, 1975; Orsi et al., 1999; Meredith et al., 2000; Gordon et al., 2001; Naveira Garabato et al., 2002). The two models show that brine rejection and surface cooling drive positive bottom water transformation while mixing with warmer WDW and fresher AAIW acts to decrease AABW. Because we cannot explicitly calculate WMT in SODA but rather infer it as a residual, it is not possible to further decompose
355   SODA's transformation into different components.

Annual mean volume budget
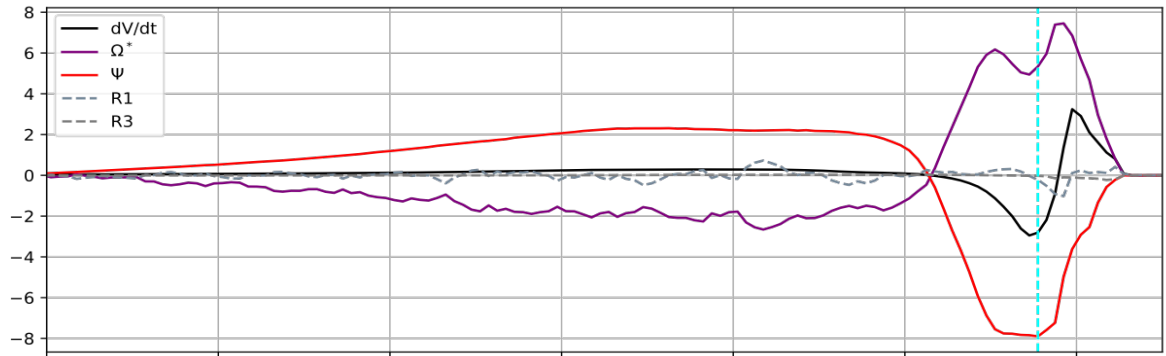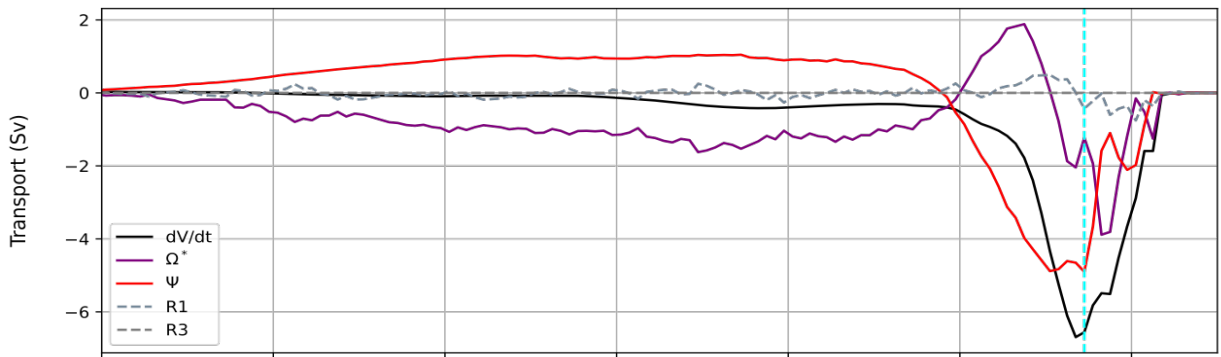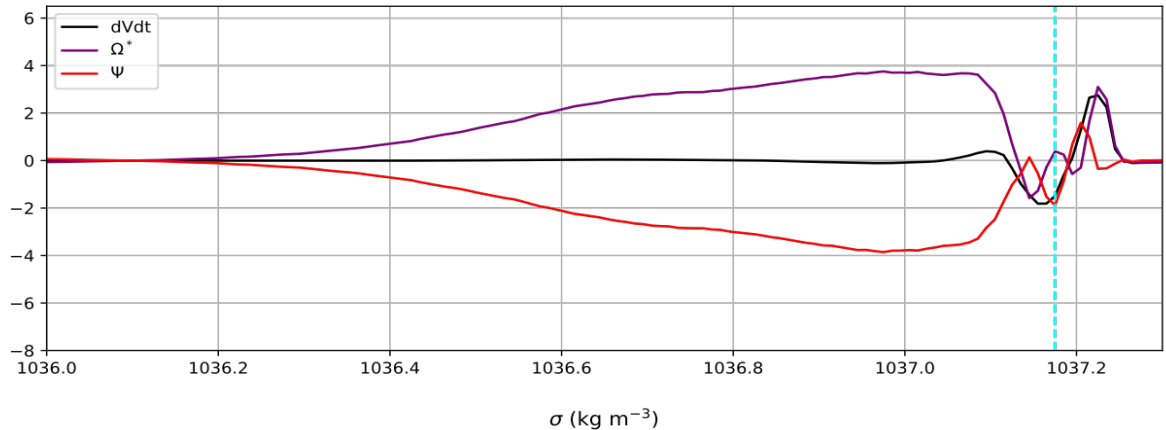
Figure 5. Main terms of the WMT-volume budget in σ space (kg m^{-3}) averaged over each model's respective time period for **(a)** ECCO (1992-2016), **(b)** SOSE (2006-2010) and **(c)** SODA (1993-2019). Volume change is represented by the black line, transport by the red line, transformation is the purple line (includes numerical mixing in ECCO and SOSE, and in SODA also includes discretization residual), and the discretization residual is explicitly shown as the grey dashed line in ECCO and SOSE. The vertical dashed line demarcates the boundary of bottom water in each model (1037.155 kg m^{-3} for ECCO, 1037.145 for SOSE, and 1037.175 kg m^{-3} for SODA).

Annual mean transformation
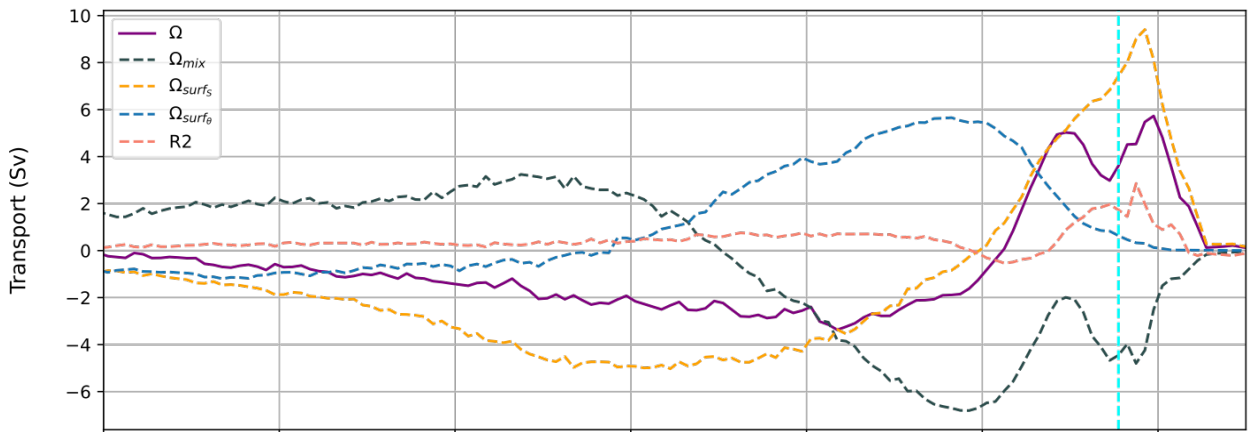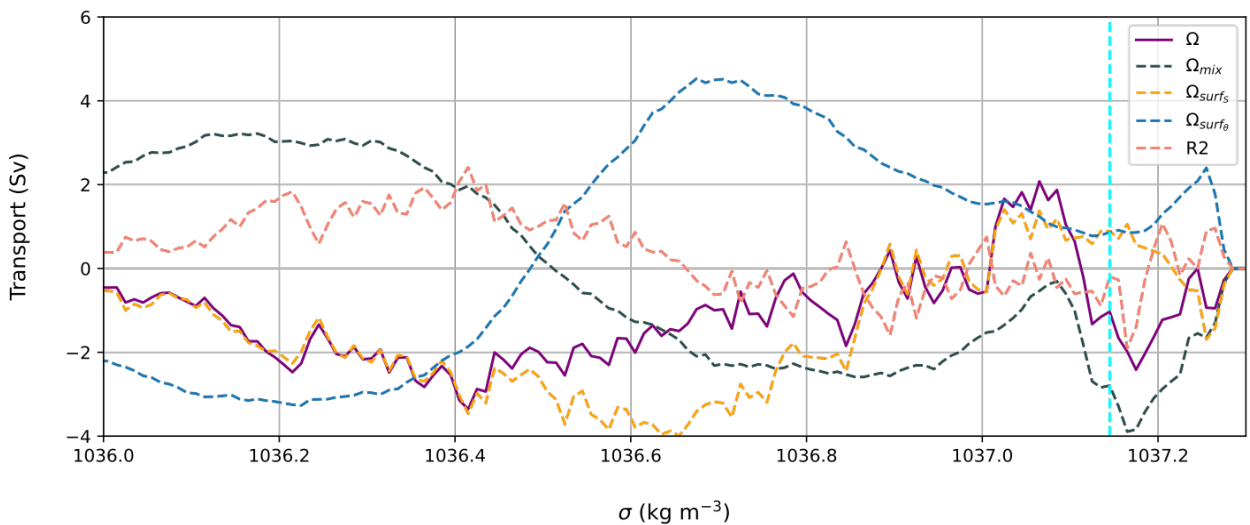
Figure 6. (a) Transformation term, Ω (purple solid line), broken down into its sources of transformation: surface salt flux (orange dashed line); surface heat flux (blue dashed line); and mixing (slate grey dashed line). Residual due to numerical mixing is the pink dashed line in ECCO (a) and SOSE (b). The vertical dashed line demarcates the boundary of bottom water in each model (1037.155 kg m^{-3} for ECCO, 1037.145 for SOSE, and 1037.175 kg m^{-}3 for SODA).

4.2 Seasonal Climatology

While the long-term annual mean shown above is what matters most for the global-scale overturning and climate, the annual mean masks a huge amount of seasonality in WMT. Exploring this seasonality is important for understanding the mechanisms behind WMT. Here we examine the monthly climatology of the transformation budget in the three models (Fig. 7 and 8). The climatology of each term was calculated as a monthly average. Figure 8 shows this climatology via contour plot and for a wider

range of densities to illustrate the seasonality across multiple water masses. For ECCO and SOSE, we also decomposed Ω into transformation from mixing, surface cooling/warming and surface freshwater fluxes in Fig. 9.

We switch to focus on a single timeseries that best represents AABW transformation and overturning, rather than the entire range of densities in Fig. 7 and 9. We do this by moving from a *transformation budget* to a *formation budget*. Again, for each model, we define the boundary between CDW (inflowing water) and AABW (outflowing water) as the density $\sigma^\dagger$ where Ψ reaches its extreme (minimum value). As stated before, the values of $\sigma^\dagger$ are 1037.155 kg m^{-3} for ECCO, 1037.145 kg m^{-3} for SOSE, and 1037.175 kg m^{-3} for SODA. By sampling Ψ, Ω, and $\partial V/\partial t$ at $\sigma^\dagger$, we obtain a single value or timeseries representing the net export rate, formation rate, and volume tendency of AABW.

In summary, the monthly view reveals that the overturning Ψ is relatively steady over the year in ECCO and SODA; in SOSE, transport shows more seasonality (Fig. 7 and 8). Next, Ω exhibits a seasonal cycle an order of magnitude larger than their annual mean. Moreover, the seasonal cycle in $\partial V/\partial t$ and Ω is largely compensatory; excess dense water is created by WMT in winter and then destroyed in summer, and a residual is left over for export from the basin via Ψ. However, in ECCO the destruction is caused by less contribution from transformation and the influence of outflow becomes compensatory.

Going into more detail with Fig. 7, we see from all three models that bottom water is gaining volume during the austral winter months and losing volume during the rest of the year. However, in SODA (Fig. 7 (c)), bottom water volume gain occurs over a longer time range, for three quarters of the year. SOSE reveals a slight imbalance between the formation rate of AABW and its export; more water is being exported over the year than is being formed. This leads to a continuous decrease in AABW volume, which we will see is the case in Sect. 5 (also visible in Fig. 5 (b)). However, superimposed upon this overall trend is a strong seasonal cycle, with excess AABW production and corresponding volume tendency in winter.

One immediately notices in SODA (Fig. 7 (c)) the overall larger monthly variability. There was also a dramatic switch between volume gain in January to significant volume loss in February (>25 Sv). SODA, as it was detailed in Sect. 3.4, differs from the other two data assimilating models in that SODA nudges the data to fit the observations it is trying to match. Such data assimilating technique commonly causes jumps in the data and produces unphysically large magnitudes in our budget terms which is consequently evident in our water mass transformation budgets. For this reason, we inserted averaged salt and temperature values from the day before and day after some of the spikes we observed in our preliminary analyses. It would help to remind the reader that the Ω^* term shown here is not quite the same as the transformation terms shown for ECCO and SOSE. The transformation term in SODA implicitly carries the residuals that were explicitly calculated in ECCO and SOSE (R1 and R2). In SODA, the advective transport of bottom water is almost insignificant compared to the large magnitude of inferred transformation. SODA still concurs with ECCO and SOSE in showing that volume gain occurs during the winter months; however, bottom water volume grows over half a year as opposed to only a few months centered in the year in ECCO and SOSE.

Looking at $\partial V/\partial t$ over a wider density range in Fig. 8, we can see in all three models that densification acts upon the lighter densities in the beginning of winter, and as the season progresses the thermodynamic process moves down to transform the denser range of the ocean. This pattern can be derived from the surface cooling component of transformation in ECCO and SOSE. This is in agreement with the general understanding that AABW in the Weddell is created when sea ice forms during the winter season, and during the warmer months the production of AABW decreases (Fig. 7 (a)) or is even being destroyed (Fig. 7

(b) and (c)). There is year-round export of bottom water in all three models, with the intensity of outflow peaking and varying in the middle of the year. Peak export happens at ~10 Sv in June in ECCO, ~12 Sv April-July in SOSE, and ~3 Sv in March in SODA. Both ECCO and SOSE values are within the error bars of Kerr et al. (2012)'s maximum monthly mean outflow value of 12.2 ± 3.0Sv.

400   Breaking down the components of Ω (Fig. 9), we can see some significant difference between ECCO and SOSE; however, note how both models exhibit broadly similar σ-temporal structure in these terms (Fig. 8 (a) and (b)), but with different magnitude and position within σ space. In ECCO (Fig. 9 (a)), the contribution of Ω^{θ}_{surf} is negligible, and Ω^{S}_{surf} is positive throughout the winter; this indicates that brine rejection is the dominant process behind AABW formation, as was seen in the annual-mean budget (Fig. 6 (a)), with little impact from ice melt, runoff, or precipitation. All the while, throughout the year, transformation

405   due to mixing is trying to homogenize the waters; therefore, bottom water is essentially being destroyed throughout the year - on the order of 4 Sv.

In SOSE (Fig. 9 (b)), AABW production during the winter months is also mainly due to brine rejection. Unlike ECCO, surface cooling provides an additional source for AABW formation in SOSE. Mixing, though more variable throughout the year in SOSE than in ECCO, still works to homogenize (destroy) bottom water. Towards the end of the winter season, Ω^{S}_{surf} is

410   negative, corresponding to ice melt.
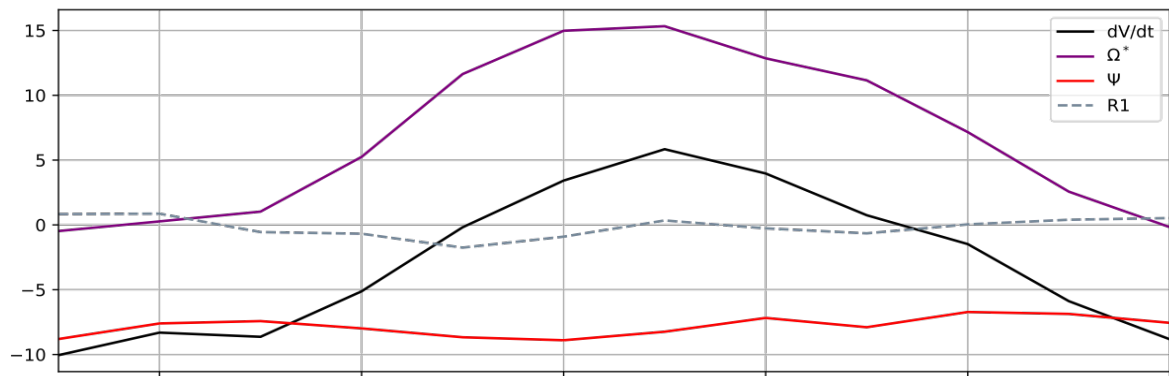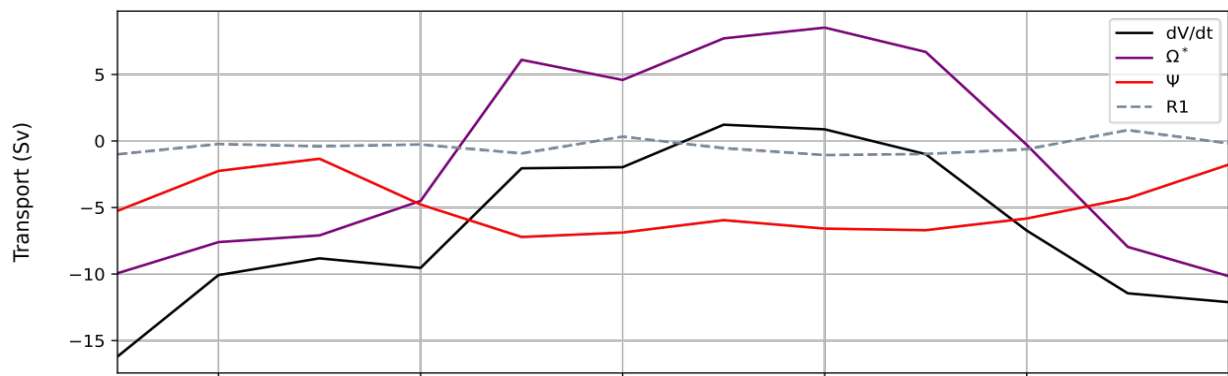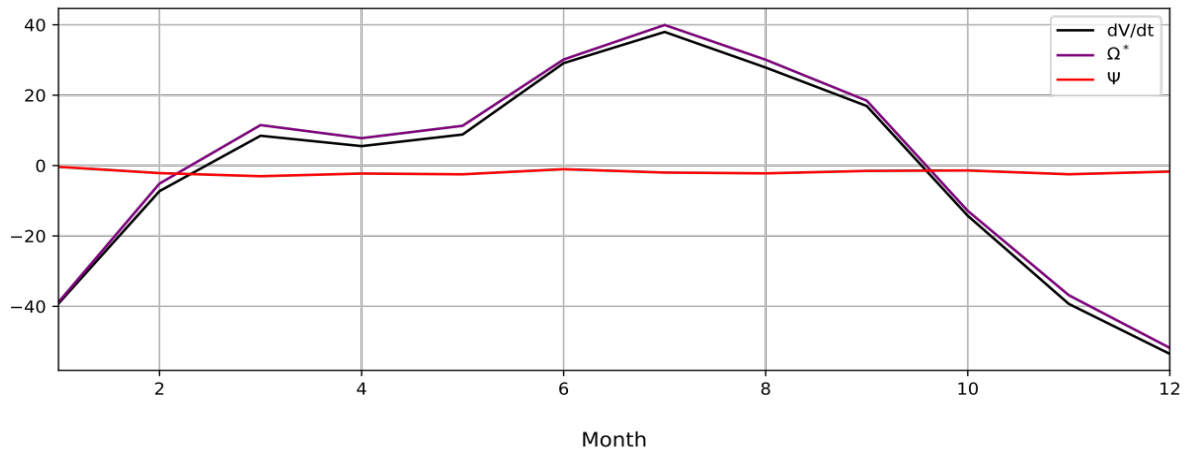
Figure 7. Monthly climatology of Weddell bottom water's main WMT budget terms in ECCO (a), SOSE (b) and SODA (c). Residual due to discretization (R1) only shown in ECCO and SOSE.
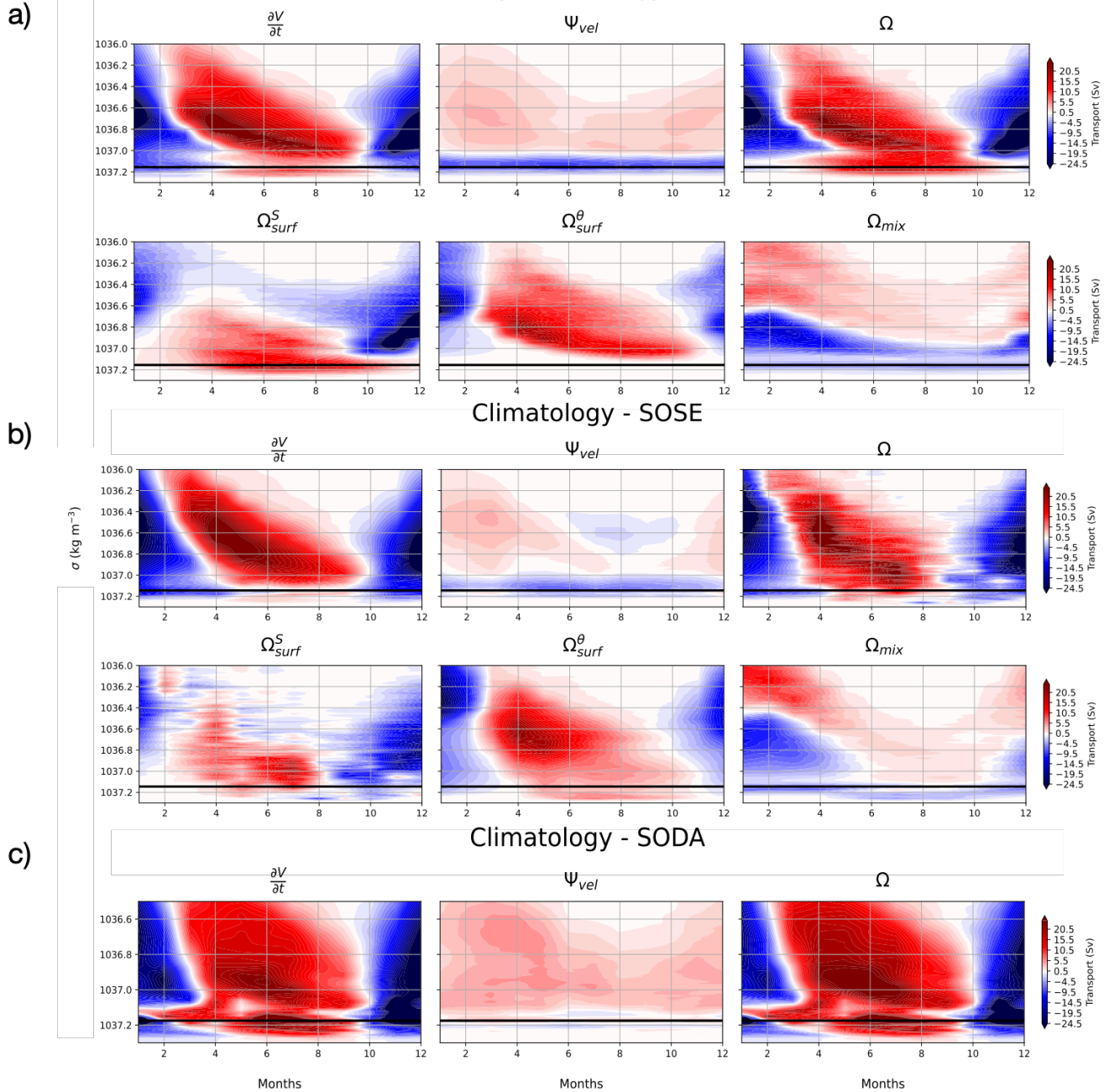
Figure 8. Monthly climatology of main WMT budget terms in top panel in ECCO (a), SOSE (b) and SODA (c); and sources of transformation (bottom panel) in ECCO (a) and SOSE (b). The horizontal black line represents the bottom water boundary in each model (1037.155 kg m^{-3} for ECCO, 1037.145 kg m^{-3} for SOSE, and 1037.175 kg m^{-3} for SODA).

Monthly climatology of transformation
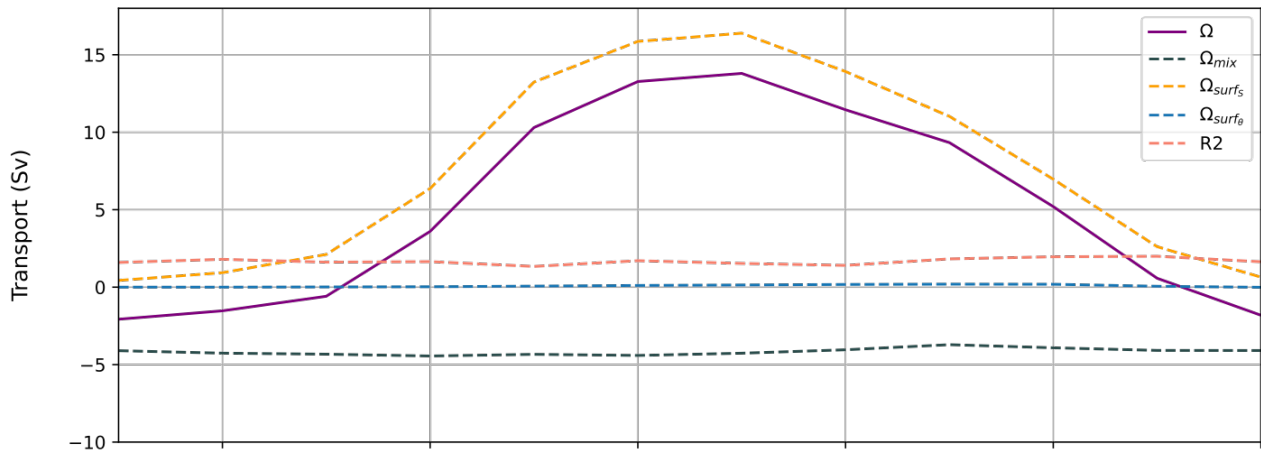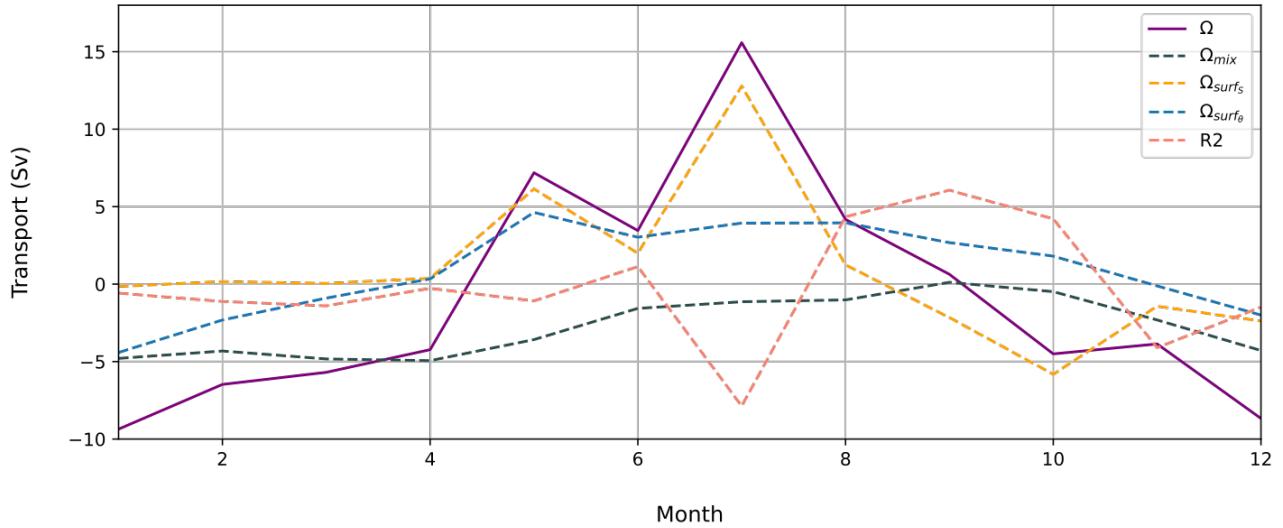
Figure 9. Monthly climatology of Weddell bottom water's transformation term (purple line), its sources of transformation: surface salt flux (orange dashed line); surface heat flux (blue dashed line); and mixing (slate grey dashed line). Residual due to numerical mixing is the pink dashed line in ECCO (a) and SOSE (b).

5 Interannual Variability

Having examined the climatology, we now turn to the main focus of our study: quantifying the interannual variability of AABW production in these reanalyses. A deep look at the interannual variability of the anomalous WMT budget terms reveals some interesting differences of AABW circulation between these three models and also serves as a point of comparison with similar

studies (Iudicone et al., 2008a, b; Abernathey et al., 2016; Gordon et al., 2020). In this section, we highlight some anomalous events and the differences between all three models.

The anomaly timeseries for each model are constructed by sampling Ψ, Ω, and $\partial V/\partial t$ at $\sigma^\dagger$, then removing the monthly climatology for each term, and smoothed by a rolling mean with the center window set to the middle of the year; these are shown in Fig. 10. For ECCO and SOSE, we also decompose Ω into components due to surface heating, surface salt flux, and interior mixing in Fig. 11. Figures 10 and 11 are thus completely analogous to Fig. 7 and 9, but for the interannual variability, rather than the seasonal cycle. The anomaly WMT timeseries each cover a different time period. SODA is the longest and provides the most recent data; the data we extracted begin in 1993 and go through 2020. ECCO begins in 1992 and extends through 2016. SOSE's time period is the shortest out of the three models; while it is the highest-resolution product analyzed here, its six-year period offers only a very limited view into interannual variability.

The most immediate feature that jumps out from Fig. 10 is the fact that the magnitude of the variability of $\partial V/\partial t$ in SODA is nearly 10x larger than ECCO and SOSE, with values as large as 75 Sv. This indicates that the volume of AABW in SODA is changing by huge amounts from year to year. These changes are not explainable by variations in overturning Ψ so they must be balanced by the inferred WMT Ω^* (recall that we cannot diagnose Ω directly from SODA but instead infer it as a residual). We hypothesize that these large-magnitude changes in AABW volume are due to SODA's data assimilation nudging the temperature and salinity fields, without a driving physical process.

The ECCO timeseries (Fig. 10(a)) reveal some degree of variability (approx. 2-4 Sv) in the WMT budget; but there is also an overall consistent relationship between terms, with anomalous transformation always positive and transport always negative. The trend in AABW variability seems to be driven mainly by transformation but its effects are constantly countered by export. In other words, the more AABW that is being formed in certain years (e.g. 1999, 2001, 2007, etc.) the more is being exported.

Digging into the decomposition of WMT terms in ECCO (Fig. 11(a)), we see, somewhat unsurprisingly, that WMT variability is largely driven by variability in surface salt fluxes. These trends are challenged by a considerable amount of mixing. The one exception to the dominant activity of surface salt fluxes on transformation is an event occurring from 2004-2008, which is associated with anomalously strong surface cooling (surface heat fluxes are otherwise negligible in the AABW budget for ECCO). Our initial assumption during this 2004-2008 period was that a polynya occurred - as is the case for SOSE in 2005. However, surface heat flux and sea ice cover maps with overlaid $\sigma_2^\dagger$ contours (not shown here) show no evidence of a simulated polynya, but do show outcropping of AABW contour in the open region of the Weddell. We also considered the possibility of a polynya with thin ice coverage. Setting the sea ice thickness threshold to be 12 cm (consistent with Nakata et al. (2021) and Mohrmann et al. (2021)) we still found no link between polynya and the AABW outcropping. We suspect that internal dynamics in ECCO drive AABW to outcrop under sea ice, where it loses heat. The heat loss due to this interaction is largely compensated by heat gain due to mixing, likely associated with convective mixing in the outcrop region.

SOSE is unique among the three models in showing a persistent trend in the WMT budget over its (relatively short) time period. As shown earlier in Fig. 5 (b), SOSE is losing AABW and gaining CDW over this time period at a rate of $\sim$10 Sv, which is mainly driven by trends in decreasing formation to ultimately increasing destruction of AABW after 2008. In the anomaly timeseries (Fig. 10 (b)), we see that this trend is not steady but in fact accelerates over time. Production of AABW (Ω)

450   is anomalously strong in the beginning of the state estimate (2005) and decreases by 16 Sv by 2010. Fig. 11 (b) shows that this decrease in production rate is driven primarily by trends in mixing, and secondly by trends in surface cooling. Surface salt fluxes do little to counter these effects. In the first year of the state estimate, an open-ocean polynya events contributes to enhancing production of AABW via surface heat fluxes; after that, there is negligible anomalous surface-heat-flux-driven production. There is some variability in production from surface salt fluxes of order 1-2 Sv. During late 2006 to 2008, transport of AABW (Ψ)

455   helps to increase volume distribution by $\sim$3 Sv (note that Fig. 10 shows the anomaly relative the climatology, not the absolute value). After that, the residual imbalance between Ψ and Ω drives an acceleration in the rate of volume loss of AABW. Overall, SOSE is the farthest of all the models from a state of balance between production and export of AABW.

Anomalous volume budget
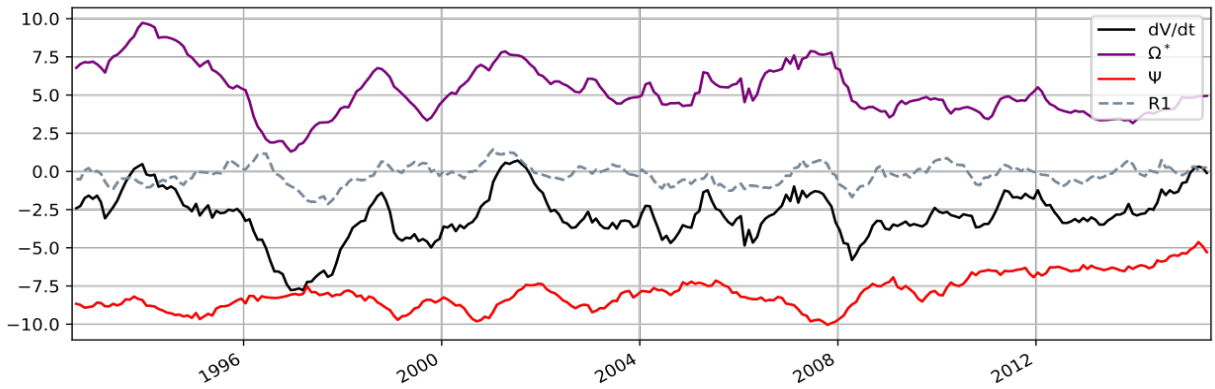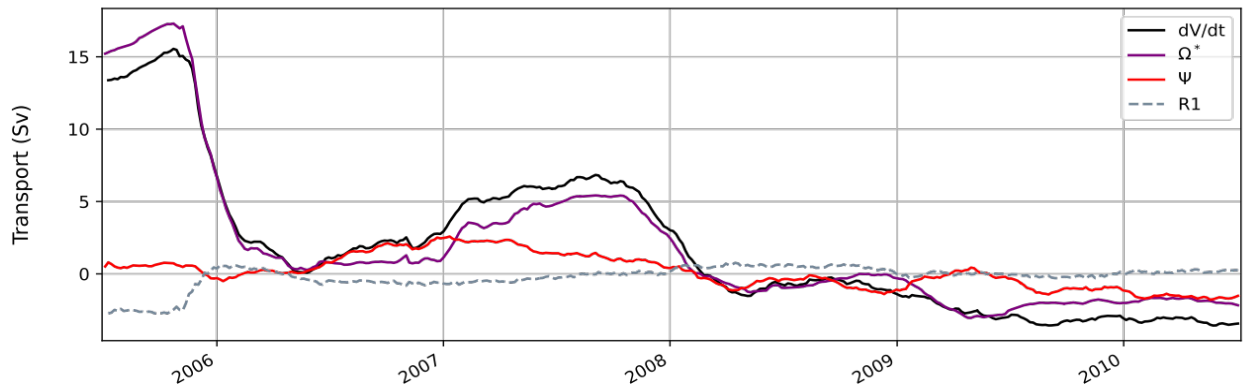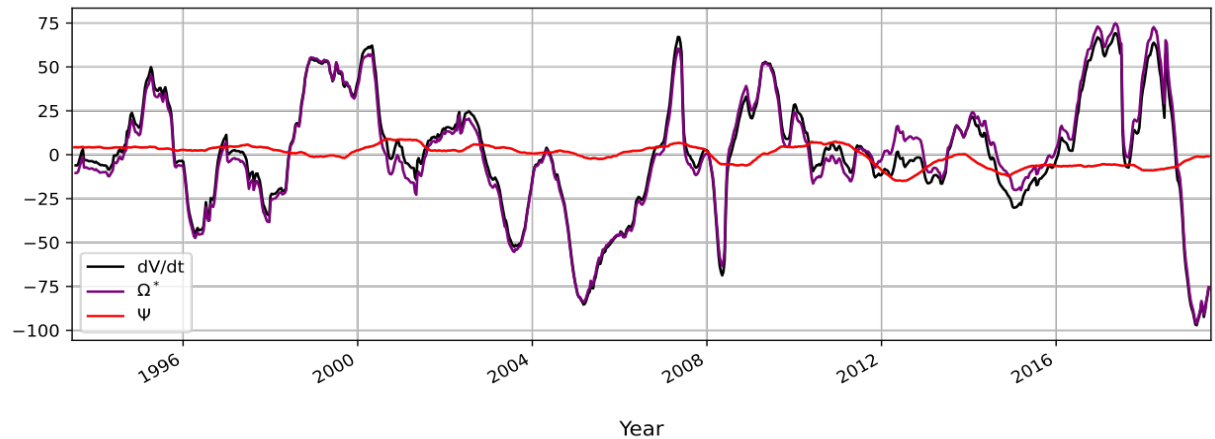
Figure 10. Anomalous main terms of WMT-volume budget in ECCO (a), SOSE (b) and SODA (c). Timeseries was smoothed by an annual rolling mean with the center window set to the middle of the year. Volume change is the black line, transport the red line, transformation is the purple line (includes R2 in ECCO and SOSE, and in SODA also includes R1 and R2), and the discretization residual is explicitly shown as the grey dashed line in ECCO and SOSE.
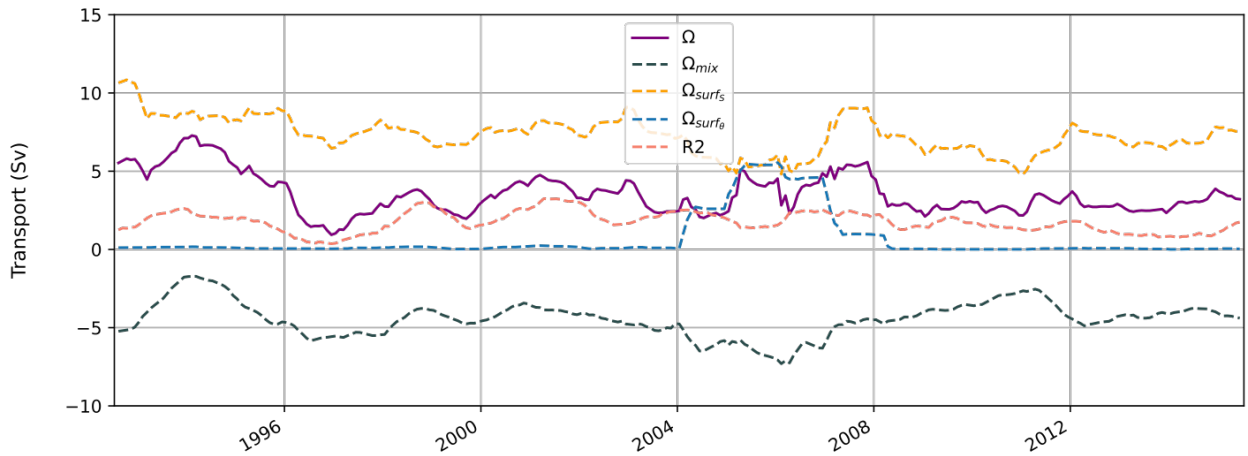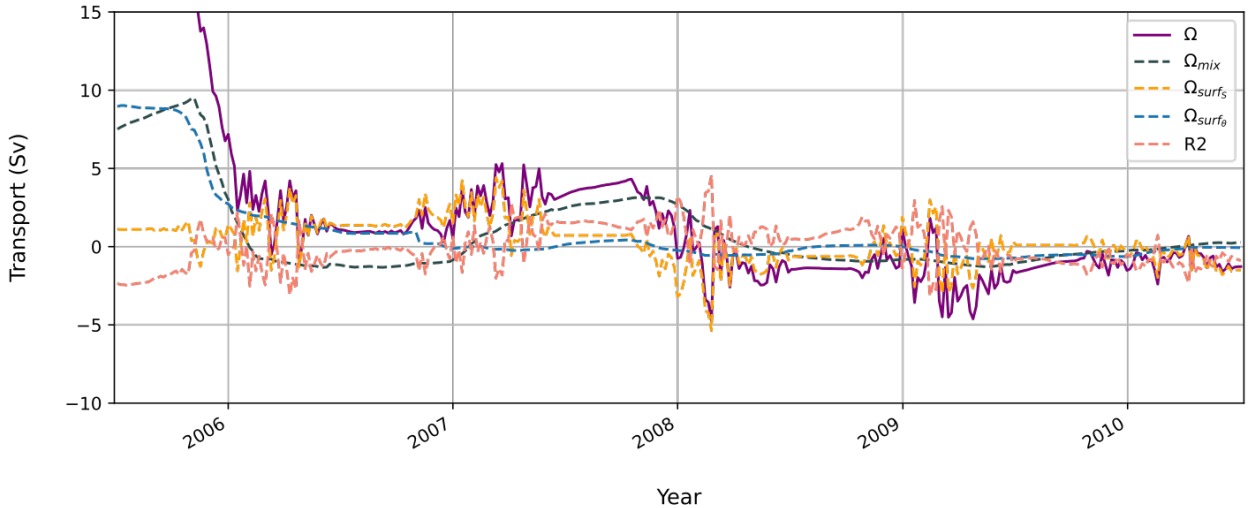
Figure 11. Anomalous transformation term, Ω (purple solid line), broken down into its sources of transformation: surface salt flux (orange dashed line); surface heat flux (blue dashed line); and mixing (slate grey dashed line). R2 is the pink dashed line.

In general, the timeseries in Fig. 10 contain many different relationships between the different budget terms in different models. To try to summarize these relationships, we compute correlations between each pair of terms. These correlations quantify the extent to which one term balances the other in a budget (Tesdal and Abernathey, 2021); for example, a correlation of 1 between $\partial V/\partial t$ and Ω means that trends in volume distribution are completely driven by anomalous water mass transformation. All reported correlation coefficients are statistically significant with a confidence level of 95 %. For ECCO (black bars), $\partial V/\partial t$ is weakly correlated with transport Ψ (0.13, p-value = 3×10^{-2}, confidence interval of 0.01 and 0.25); and strongly correlated
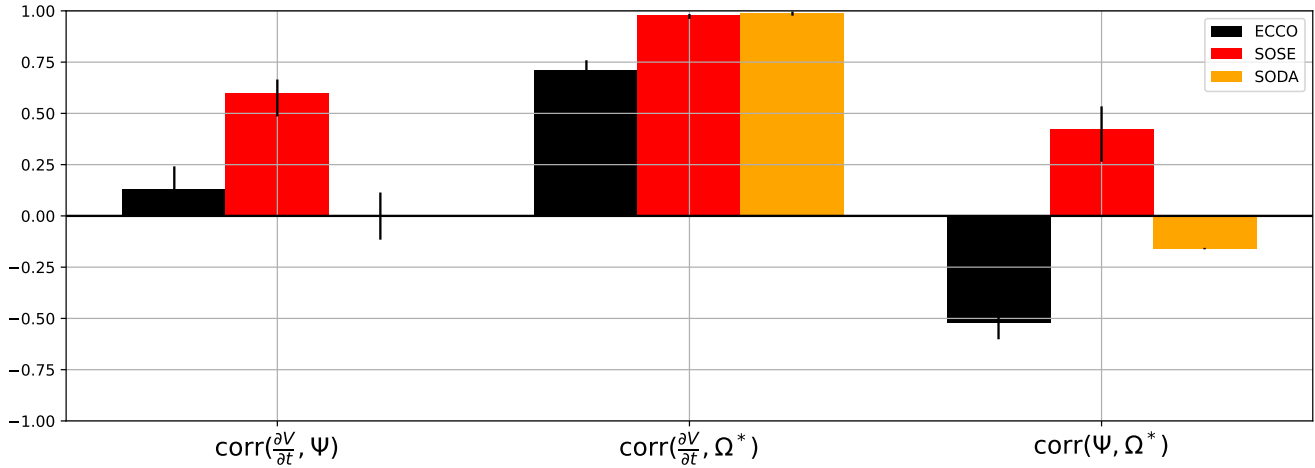
Figure 12. Correlation (and associated error bars) between the main budget terms from each model. The bars in black represent the correlation values in ECCO, red in SOSE and orange in SODA.

with transformation (0.71, p-value = 2×10^{-43}, confidence interval of 0.65 and 0.76), indicating a dominant compensation

465 of transformation on $\partial V / \partial t$. The correlation between Ψ and Ω is negative (-0.52, p-value = 1×10^{-20}, confidence interval of -0.60 and -0.43). In SOSE (red bars), there is a positive correlation between transformation and transport (0.70, p-value = 2×10^{-9}, confidence interval of 0.54 and 0.82). Similar to ECCO, there is a stronger relationship between trends in volume and transformation (0.98, p-value = 2×10^{-38}, confidence interval of 0.96 and 0.99) relative to transport (0.82, p-value = 1×10^{-14}, confidence interval of 0.71 and 0.89); in SOSE, volume trends in AABW are driven by variability in both transformation

470 and transport. Finally, in SODA (orange bars), variability is completely driven by transformation (0.99, p-value = 1×10^{-201}, confidence interval of 0.98 and 0.99), and has no relationship to transport (0, p-value = 3×10^{-3}, confidence interval of 0 and 0.06). There is a weak anti-correlation between transport and transformation (-0.16, p-value = 1, confidence interval of -0.12 and 0.12). Overall, the correlation analysis confirms what is seen visually in the timeseries; each reanalysis has a different overall relationship between WMT budget terms, yet they all show a positive and stronger relationship between $\partial V / \partial t$ and Ω than

475 between $\partial V / \partial t$ and Ψ.

Many studies have argued for links between large-scale climate indices and AABW production / export (Gordon et al., 2007; Meredith et al., 2008; Gordon et al., 2010; McKee et al., 2011; Gordon et al., 2020). We examined this in the three reanalyses by calculating correlations between the terms in the WMT budgets and climate forcings from El Niño Southern Oscillation (ENSO), the Southern Annular Mode (SAM), wind stress curl (WSC) and sea ice concentration (SIC). ENSO data was taken

480 from the NOAA Extended Reconstructed Sea Surface Temperature (ERSST) version 5 project (Huang et al., 2017). The SAM index was obtained from Marshall and National Center for Atmospheric Research Staff (2021). Windstress curl was calculated from ERA-Interim zonal wind stress state variables (Dee et al., 2011), and finally, for sea ice concentration we used each

model's sea ice concentration diagnostic averaged over the WG region. We standardized each index by dividing the anomaly timeseries by their respective standard deviation in time. Notable correlation values in SOSE are between all the budget terms and SIC: $\partial V/\partial t$ and SIC (-0.60, p-value = 1×10^{-6}, confidence interval of -0.74 and -0.40); Ψ and SIC (-0.70, p-value = 5×10^{-9}, confidence interval of -0.81 and -0.52); and Ω and SIC (-0.53, p-value = 3×10^{-5}, confidence interval of -0.70 and -0.31). Additionally, observed between all three budget terms and WSC were positive correlations: $\partial V/\partial t$ and SIC (0.33, p-value = 1×10^{-2}, confidence interval of 0.07 and 0.55); Ψ and SIC (0.34, p-value = 1×10^{-2}, confidence interval of 0.08 and 0.55); and Ω and SIC (0.33, p-value = 2×10^{-2}, confidence interval of 0.07 and 0.54). In SODA, transport is negatively correlated with SIC (-0.46, p-value = 2×10^{-15}, confidence interval of -0.55 and -0.36). In ECCO, there were no notable correlation between budget terms and climate indices.

6 Discussion & Conclusion

Overall, the main contribution of our study is to diagnose, for the first time, a closed, time-dependent water mass budget for AABW in the Weddell Sea from three state-of-the-art ocean reanalyses. This gives an unprecedented view into the processes that control the volume, production, and export of AABW from this climatically important region. In the long-term annual mean, all three models produce and export AABW at rates broadly compatible with observations. However, there is little agreement between these reanalysis products on interannual timescales.

We now summarize some of the main features of the AABW volume budget timeseries in each reanalysis. SODA showed an extreme amount of variability in AABW volume in the WG which could not be explained by variations in export. Although we could not diagnose WMT explicitly in SODA due to its lack of closed heat and salt budgets, the only possible explanation for this variability is WMT, likely driven by the nudging tendencies of the data assimilation scheme. The obvious conclusion is that reanalyses based on 3DVar data assimilation are not suitable for WMT studies, since they are not constrained to actually conserve heat and salt. Due to their adjoint-based data assimilation, ECCO and SOSE do provide such closed budgets, and therefore can provide better insight into the drivers of variability in WMT. Both models show strong interannual variability in the AABW volume budget. SOSE's short time period makes it hard to draw general conclusions; during this time period there is an accelerating loss of AABW, driven largely by interior mixing and changes in surface salt fluxes. The transformation changes are paired with a weaker influence from export. Given the short time period of SOSE, these trends may simply be a part of low frequency interannual variability. Indeed ECCO does display such interannual variability; there are numerous 5-year periods that show secular trends in one or more terms. Moreover, there is some indication of alignment in these trends between ECCO and SOSE, particularly the strong decline in AABW production from 2007 - 2010. In our assessment, ECCO provides the most useful timeseries for revealing the processes and mechanisms that drive WMT and export variability. It exhibits interannual fluctuations offset by its mean state with a reasonable magnitude relative to the climatology. The decomposition of WMT in ECCO reveals a rich interplay between variability in export, surface forcing, and interior mixing in driving AABW volume variability.

515 Because of the difficulty of observing the deep outflow of AABW, it would be very useful if we could relate AABW export to surface processes in the Weddell Sea. Gordon et al. (2020) showed strong interannual variability in Weddell Sea Bottom Water salinity, as measured by nearly 20 years of mooring data in the northwest Weddell basin. They made the case that this variability was tied to the strength of the WG and ultimately the wind stress curl, which is influenced by large-scale climate modes such as ENSO and SAM. In a similar vein, Kerr et al. (2012) found a strong co-varying relationship between bottom water transport

520 and brine rejection in a 20-year high-resolution numerical simulation. We searched for such relationships in ECCO and SOSE. We found transport in SOSE to be strongly correlated with: surface-salt-flux-induced transformation (0.66, p-value = 4×10^{-8}, confidence interval of 0.48 and 0.79); weakly correlated with surface heat-flux-induced transformation (0.28, p-value = 4×10^{-2}, confidence interval of 0.02 and 0.51); as well as with mixing-induced transformation (0.27, p-value = 4×10^{-2}, confidence interval of 0.01 and 0.50). Both this study and Kerr et al. (2012) find that salt fluxes near the surface and bottom water export

525 co-vary as they are both directly influenced by wind forcings that influence WG strength. We found the windstress curl over the WG region to be most correlated with the surface salt flux source of transformation, though the relationship is indeed weak (0.28, p-value = 4×10^{-2}, confidence interval of 0.02 and 0.51) in SOSE. However, SOSE is very short, so these correlations are not definitive. In contrast, the only notable relationship between transport and the different sources of transformation in ECCO was between Ψ and surface-salt-flux-induced transformation (-0.44, p-value = 3×10^{-14}, confidence interval of -0.53 and -0.34).

530 We note the importance of the volume tendency term $\partial V / \partial t$ in the WMT budget. When this term is large, it means that excess AABW production need not correspond with export; instead, it can drive large trends in the water mass distribution within the basin, without any impact on export. Over its 25-year timeseries, the relationship between the terms in the WMT budget changes dynamically, with no clear dominant balance. This complexity confounds the goal of establishing a simple relationship between surface forcing and AABW export. This is an important insight for studies of the WG based on surface and satellite-based

535 observations.

  Numerous studies have shown that AABW in the Weddell Sea has been warming (Robertson et al., 2002; Fahrbach et al., 2004; Purkey and Johnson, 2010; Fahrbach et al., 2011; Meredith et al., 2011; Couldrey et al., 2013), freshening (Jullion et al., 2013), and losing volume (Purkey and Johnson, 2012; Kerr et al., 2018). Purkey and Johnson (2012) suggest that the decline in AABW production by a rate of -8.2 ($\pm$2.6Sv) is the cause for the contraction of bottom water volume for the period 1993-2006.

540 As shown in the annual mean (Fig. 5), all three models are losing AABW volume, with SOSE losing AABW much faster. In all three models, the decline in AABW is due to an imbalance between AABW formation and export; the models export more AABW than they produce. In ECCO, the volume loss is roughly steady over 25 years, with significant interannual variability. In SOSE, in contrast, it accelerates strongly over the 6-year period.

  In Hellmer et al. (2011), it is hypothesized that the freshening of the northwest shelf water contributing to an increase in

545 glacial meltwater input is the cause of the slowdown of AABW production rate. Surface freshening makes it more difficult for surface and shelf waters to sink which slows the production of AABW and subsequently, the circulation of the lower limb of the MOC. In SOSE, Fig. 11 (b), there is a declining trend in transformation, partly due to a switch from brine rejection inducing formation prior to mid-2008, to freshwater input causing AABW destruction from 2008 to mid-2009 and stays roughly near zero thereafter. Since SOSE does not include time-variable runoff, such trends must be due to variations in sea ice. In ECCO, we

do not see such a trend in transformation nor in freshwater flux-sourced transformation to suggest a decline in AABW volume
due to freshening.

Our project has sought to explore how current state of the art data-assimilating ocean reanalyses can help fill the gaps in our
understanding of the thermodynamic drivers of AABW export variability from the Weddell Sea; specifically, the quantitative
links between surface forcing, interior dynamic and thermodynamic processes, and outflow. From the WMT analysis employed
with the three ocean state estimates, we have determined that the variability of AABW is driven by a combination of surface
forcings derived from strong winds and brine rejection and interior diapycnal mixing. An additional initial goal of our work was
to probe the mechanistic link between climate forcings, SAM and ENSO, and AABW transformation and export, as has been
suggested by observations (Gordon et al., 2020). However, none of the reanalyses we analyzed exhibited such clear links. We
further had hoped that, since these reanalyses assimilate data and aim to capture the real history of the ocean state, they might
simulate the specific phasing of interannual variability seen in the mooring records (Gordon et al., 2020); however, this was not
the case. The discrepancies between the models, and between the models and observations, suggest that this class of reanalyses
is not capable of consistently and faithfully capturing the processes that drive AABW variability in a robust way. Similar to
the conclusions of Heuzé et al. (2013) and Heuzé (2021) regarding CMIP5 and CMIP6 models, respectively, the relatively
coarse resolution of these models makes it difficult to resolve processes such as coastal polynyas, dense overflows, and the sharp,
v-shaped front of the western boundary current which Gordon et al. (2020) argued was crucial for the pathway of AABW export.

Regardless of these shortcomings, we feel that the time-dependent water mass framework presented here is a useful tool
for understanding AABW variability in this region. A very promising direction for future work would be to apply the same
methodology to higher-resolution models, which presumably represent small scale processes with much greater fidelity. A recent
study by Stewart (2021) showed that a $1/12°$ regional model of the Weddell Sea could resolve the impact of tides and eddies
on cross-shelf transfer of buoyancy, resulting in a more realistic overturning circulation. High resolution global ocean climate
models (e.g. Small et al., 2014; Morrison et al., 2016; Kiss et al., 2020) are also capable of resolving these processes in better
detail and would be a promising tool for investigating AABW WMT. One challenge, however, in applying the WMT approach
to these models is the computationally demanding nature of the WMT diagnostics, which require closed heat and salt budgets to
begin with, and then layer on additional complex calculations.

We also note the limitations of the potential-density WMT framework used here. Our method is not capable of explicitly
diagnosing WMT effects due to the nonlinear equation of state—cabbeling and thermobaricity—even those processes are
hypothesized to be important for the transformation of water masses to become AABW (Gill, 1973; Gordon et al., 2020;
Mohrmann et al., 2022). Alternative frameworks use neutral density (Jackett and McDougall, 1997; Iudicone et al., 2008b) or
move to two-dimensional temperature / salinity water-mass coordinates (Evans et al., 2018), which can reveal subtleties in the
transformation process that are inaccessible to the 1D density-based approach. We look forward to exploring these possibilities
in future work.

Code and data availability.

WMT budgets can be found in the author's *GitHub repository*. The analysis-ready datasets used for calculating the budgets can be found in the cloud through *Pangeo's catalog*.

585 *Author contributions.*

Shanice Bailey and Ryan Abernathey conceptualized the research goals. Shanice Bailey conducted the analysis with help from Spencer Jones and Ryan Abernathey. Shanice Bailey prepared the manuscript with significant contributions from all coauthors. Arnold Gordon and Xiaojun Yuan provided scientific input and guidance.

B Special issue statement

590 This manuscript is also being submitted for the Special Issue on the Weddell Sea hosted by the Southern Ocean Observing System Weddell Sea Dronning Maud Land Regional Working Group.

References

Abernathey, R. P., Cerovecki, I., Holland, P. R., Newsom, E., Mazloff, M., and Talley, L. D.: Water-mass transformation by sea ice in the upper branch of the Southern Ocean overturning, Nature Geoscience, 9, 596–601, https://doi.org/10.1038/ngeo2749, 2016.

Armitage, T. W. K., Kwok, R., Thompson, A. F., and Cunningham, G.: Dynamic Topography and Sea Level Anomalies of the Southern Ocean: Variability and Teleconnections, Journal of Geophysical Research: Oceans, 123, 613–630, https://doi.org/https://doi.org/10.1002/2017JC013534, 2018.

Brown, P. J., Jullion, L., Landschützer, P., Bakker, D. C. E., Naveira Garabato, A. C., Meredith, M. P., Torres-Valdés, S., Watson, A. J., Hoppema, M., Loose, B., Jones, E. M., Telszewski, M., Jones, S. D., and Wanninkhof, R.: Carbon dynamics of the Weddell Gyre, Southern Ocean, Global Biogeochemical Cycles, 29, 288–306, https://doi.org/https://doi.org/10.1002/2014GB005006, 2015.

Buckley, M., Campin, J.-M., Chaudhuri, A., Fenty, I., Forget, G., Fukumori, I., Heimbach, P., Hill, C., King, C., Liang, X., Nguyen, A., Piecuch, C., Ponte1, R., Quinn, K., Sonnewald, M., Spiege, D., Vinogradova, N., Wang, O., and Wunsch, C.: The ECCO Consortium: A Twenty-Year Dynamical Oceanic Climatology: 1994-2013. Part 2: Velocities, Property Transports, Meteorological Variables, Mixing Coefficients, 2017.

Carmack, E. C.: A quantitative characterization of water masses in the Weddell sea during summer, Deep Sea Research and Oceanographic Abstracts, 21, 431–443, https://doi.org/https://doi.org/10.1016/0011-7471(74)90092-8, 1974.

Carmack, E. C. and Foster, T. D.: On the flow of water out of the Weddell Sea, Deep Sea Research and Oceanographic Abstracts, 22, 711–724, https://doi.org/https://doi.org/10.1016/0011-7471(75)90077-7, 1975.

Carton, J. A., Chepurin, G. A., and Chen, L.: SODA3: A New Ocean Climate Reanalysis, Journal of Climate, 31, 6967 – 6983, https://doi.org/10.1175/JCLI-D-18-0149.1, 2018.

Carton, J. A., Penny, S. G., and Kalnay, E.: Temperature and Salinity Variability in the SODA3, ECCO4r3, and ORAS5 Ocean Reanalyses, 1993–2015, Journal of Climate, 32, 2277 – 2293, https://doi.org/10.1175/JCLI-D-18-0605.1, 2019.

Couldrey, M. P., Jullion, L., Naveira Garabato, A. C., Rye, C., Herráiz-Borreguero, L., Brown, P. J., Meredith, M. P., and Speer, K. L.: Remotely induced warming of Antarctic Bottom Water in the eastern Weddell gyre, Geophysical Research Letters, 40, 2755–2760, https://doi.org/https://doi.org/10.1002/grl.50526, 2013.

Dee, D. P., Uppala, S. M., Simmons, A. J., Berrisford, P., Poli, P., Kobayashi, S., Andrae, U., Balmaseda, M. A., Balsamo, G., Bauer, P., Bechtold, P., Beljaars, A. C. M., van de Berg, L., Bidlot, J., Bormann, N., Delsol, C., Dragani, R., Fuentes, M., Geer, A. J., Haimberger, L., Healy, S. B., Hersbach, H., Hólm, E. V., Isaksen, L., Kållberg, P., Köhler, M., Matricardi, M., McNally, A. P., Monge-Sanz, B. M., Morcrette, J.-J., Park, B.-K., Peubey, C., de Rosnay, P., Tavolato, C., Thépaut, J.-N., and Vitart, F.: The ERA-Interim reanalysis: configuration and performance of the data assimilation system, Quarterly Journal of the Royal Meteorological Society, 137, 553–597, https://doi.org/https://doi.org/10.1002/qj.828, 2011.

Delworth, T. L., Rosati, A., Anderson, W., Adcroft, A. J., Balaji, V., Benson, R., Dixon, K., Griffies, S. M., Lee, H.-C., Pacanowski, R. C., Vecchi, G. A., Wittenberg, A. T., Zeng, F., and Zhang, R.: Simulated Climate and Climate Change in the GFDL CM2.5 High-Resolution Coupled Climate Model, Journal of Climate, 25, 2755 – 2781, https://doi.org/10.1175/JCLI-D-11-00316.1, 2012.

Evans, D. G., Zika, J. D., Naveira Garabato, A. C., and Nurser, A. J. G.: The Cold Transit of Southern Ocean Upwelling, Geophysical Research Letters, 45, 13,386–13,395, https://doi.org/https://doi.org/10.1029/2018GL079986, 2018.

Fahrbach, E., Hoppema, M., Rohardt, G., Schroder, M., and Wisotzki, A.: Decadal-scale variations of water mass properties in the deep Weddell Sea, Ocean Dyn., 54, 77–91, 2004.

Fahrbach, E., Hoppema, M., Rohardt, G., Boebel, O., Klatt, O., and Wisotzki, A.: Warming of deep and abyssal water masses along the
Greenwich meridian on decadal time scales: The Weddell gyre as a beat buffer, Deep-Sea Res. II, 58, 2508–2523, 2011.

Ferrari, R., Jansen, M. F., Adkins, J. F., Burke, A., Stewart, A. L., and Thompson, A. F.: Antarctic sea ice control on ocean cir-
culation in present and glacial climates, Proceedings of the National Academy of Sciences of the United States of America,
https://doi.org/https://doi.org/10.1073/pnas.1323922111, 2014.

Forget, G., Campin, J.-M., Heimbach, P., Hill, C. N., Ponte, R. M., and Wunsch, C.: ECCO version 4: an integrated framework for non-linear
inverse modeling and global ocean state estimation, Geoscientific Model Development, 8, 3071–3104, https://doi.org/10.5194/gmd-8-3071-
2015, 2015.

Fukumori, I., Fenty, I. Forget, G., Heimbach, P., King, C., Nguyen, A., Piecuch, P., Ponte, R., Quinn, K., Vinogradova, N., and Wang, O.: Data
sets used in ECCO Version 4 Release 3, 2018.

Gill, A.: Circulation and bottom water production in the Weddell Sea, Deep Sea Research and Oceanographic Abstracts, 20, 111–140,
https://doi.org/https://doi.org/10.1016/0011-7471(73)90048-X, 1973.

Gordon, A. L., Visbeck, M., and Huber, B.: Export of Weddell Sea deep and bottom water, Journal of Geophysical Research: Oceans, 106,
9005–9017, https://doi.org/https://doi.org/10.1029/2000JC000281, 2001.

Gordon, A. L., Visbeck, M., and Comiso, J. C.: A Possible Link between the Weddell Polynya and the Southern Annular Mode, Journal of
Climate, 20, 2558 – 2571, https://doi.org/10.1175/JCLI4046.1, 2007.

Gordon, A. L., Huber, B., McKee, D., and Visbeck, M.: A seasonal cycle in the export of bottom water from the Weddell Sea, Nature
Geoscience, 3, 551–556, https://doi.org/10.1038/ngeo916, 2010.

Gordon, A. L., Huber, B. A., and Abrahamsen, E. P.: Interannual Variability of the Outflow of Weddell Sea Bottom Water, Geophysical
Research Letters, 47, e2020GL087 014, https://doi.org/https://doi.org/10.1029/2020GL087014, e2020GL087014 2020GL087014, 2020.

Groeskamp, S., Abernathey, R. P., and Klocker, A.: Water mass transformation by cabbeling and thermobaricity, Geophysical Research Letters,
43, 10,835–10,845, https://doi.org/https://doi.org/10.1002/2016GL070860, 2016.

Groeskamp, S., Griffies, S. M., Iudicone, D., Marsh, R., Nurser, A. G., and Zika, J. D.: The Water Mass Transformation Framework for Ocean
Physics and Biogeochemistry, Annual Review of Marine Science, 11, 271–305, https://doi.org/10.1146/annurev-marine-010318-095421,
pMID: 30230995, 2019.

Hellmer, H., Huhn, O., Gomis, D., and Timmermann, R.: On the freshening of the northwestern Weddell Sea continental shelf, Ocean Sci., 7,
305–316, 2011.

Heuzé, C.: Antarctic Bottom Water and North Atlantic Deep Water in CMIP6 models, Ocean Science, 17, 59–90, https://doi.org/10.5194/os-
17-59-2021, 2021.

Heuzé, C., Heywood, K. J., Stevens, D. P., and Ridley, J. K.: Southern Ocean bottom water characteristics in CMIP5 models, Geophysical
Research Letters, 40, 1409–1414, https://doi.org/https://doi.org/10.1002/grl.50287, 2013.

Holmes, R. M., Zika, J. D., Griffies, S. M., Hogg, A. M., Kiss, A. E., and England, M. H.: The Geography of Numer-
ical Mixing in a Suite of Global Ocean Models, Journal of Advances in Modeling Earth Systems, 13, e2020MS002 333,
https://doi.org/https://doi.org/10.1029/2020MS002333, e2020MS002333 2020MS002333, 2021.

Huang, B., Thorne, P. W., Banzon, V. F., Boyer, T., Chepurin, G., Lawrimore, J. H., Menne, M. J., Smith, T. M., Vose, R. S., and Zhang, H.-M.:
Extended Reconstructed Sea Surface Temperature, Version 5 (ERSSTv5): Upgrades, Validations, and Intercomparisons, Journal of Climate,
30, 8179 – 8205, https://doi.org/10.1175/JCLI-D-16-0836.1, 2017.

Ito, T., Bracco, A., Deutsch, C., Frenzel, H., Long, M., and Takano, Y.: Sustained growth of the Southern Ocean carbon storage in a warming climate, Geophysical Research Letters, 42, 4516–4522, https://doi.org/https://doi.org/10.1002/2015GL064320, 2015.

Iudicone, D., Madec, G., Blanke, B., and Speich, S.: The Role of Southern Ocean Surface Forcings and Mixing in the Global Conveyor, Journal of Physical Oceanography, 38, 1377 – 1400, https://doi.org/10.1175/2008JPO3519.1, 2008a.

670 Iudicone, D., Madec, G., and McDougall, T. J.: Water-Mass Transformations in a Neutral Density Framework and the Key Role of Light Penetration, Journal of Physical Oceanography, 38, 1357 – 1376, https://doi.org/10.1175/2007JPO3464.1, 2008b.

Jackett, D. R. and Mcdougall, T. J.: Minimal Adjustment of Hydrographic Profiles to Achieve Static Stability, Journal of Atmospheric and Oceanic Technology, 12, 381 – 389, https://doi.org/10.1175/1520-0426(1995)012<0381:MAOHPT>2.0.CO;2, 1995.

Jackett, D. R. and McDougall, T. J.: A Neutral Density Variable for the World's Oceans, Journal of Physical Oceanography, 27, 237 – 263, 675 https://doi.org/10.1175/1520-0485(1997)027<0237:ANDVFT>2.0.CO;2, 1997.

Johnson, G. C.: Quantifying Antarctic Bottom Water and North Atlantic Deep Water volumes, Journal of Geophysical Research: Oceans, 113, https://doi.org/https://doi.org/10.1029/2007JC004477, 2008.

Jullion, L., Garabato, A. C. N., Meredith, M. P., Holland, P. R., Courtois, P., and King, B. A.: Decadal Freshening of the Antarctic Bottom Water Exported from the Weddell Sea, Journal of Climate, 26, 8111 – 8125, https://doi.org/10.1175/JCLI-D-12-00765.1, 2013.

680 Kerr, R., Heywood, K. J., Mata, M. M., and Garcia, C. A. E.: On the outflow of dense water from the Weddell and Ross Seas in OCCAM model, Ocean Science, 8, 369–388, https://doi.org/10.5194/os-8-369-2012, 2012.

Kerr, R., Dotto, T. S., Mata, M. M., and Hellmer, H. H.: Three decades of deep water mass investigation in the Weddell Sea (1984–2014): Temporal variability and changes, Deep Sea Research Part II: Topical Studies in Oceanography, 149, 70–83, https://doi.org/https://doi.org/10.1016/j.dsr2.2017.12.002, oceanographic processes and biological responses around Northern Antarctic 685 Peninsula: a 15-year contribution of the Brazilian High Latitude Oceanography Group, 2018.

Kiss, A. E., Hogg, A. M., Hannah, N., Boeira Dias, F., Brassington, G. B., Chamberlain, M. A., Chapman, C., Dobrohotoff, P., Domingues, C. M., Duran, E. R., England, M. H., Fiedler, R., Griffies, S. M., Heerdegen, A., Heil, P., Holmes, R. M., Klocker, A., Marsland, S. J., Morrison, A. K., Munroe, J., Nikurashin, M., Oke, P. R., Pilo, G. S., Richet, O., Savita, A., Spence, P., Stewart, K. D., Ward, M. L., Wu, F., and Zhang, X.: ACCESS-OM2 v1.0: a global ocean–sea ice model at three resolutions, Geoscientific Model Development, 13, 401–442, 690 https://doi.org/10.5194/gmd-13-401-2020, 2020.

Levitus, S., Boyer, T. P., García, H. E., Locarnini, R. A., Zweng, M. M., Mishonov, A. V., Reagan, J. R., Antonov, J. I., Baranova, O. K., Biddle, M., Hamilton, M., Johnson, D. R., Paver, C. R., and Seidov, D.: 2014.

Locarnini, R. A., Mishonov, A. V., Antonov, J. I., T. P. Boyer, H. E. García, O. K. B. M. M. Z. C. R. P. J. R. R. D. R. J. M. H., and Seidov, D.: World Ocean Atlas 2013, Volume 1: Temperature. S. Levitus, Ed., A. Mishonov Technical Ed.; NOAA Atlas NESDIS, 73, 40, 2013.

695 Mackensen, A., Hubberten, H. W., Scheele, N., and Schlitzer, R.: Decoupling of $\delta13C\Sigma CO_2$ and phosphate in recent Weddell Sea deep and bottom water: Implications for glacial Southern Ocean paleoceanography, Paleoceanography, 11, 203–215, https://doi.org/https://doi.org/10.1029/95PA03840, 1996.

Marshall, G. and National Center for Atmospheric Research Staff, E.: The Climate Data Guide: Marshall Southern Annular Mode (SAM) Index (Station-based), https://climatedataguide.ucar.edu/climate-data/marshall-southern-annular-mode-sam-index-station-based, 2021.

700 Mazloff, M. and National Center for Atmospheric Research Staff, E.: The Climate Data Guide: Southern Ocean State Estimate (SOSE), https://climatedataguide.ucar.edu/climate-data/southern-ocean-state-estimate-sose, 2021.

Mazloff, M. R.: The dynamics of the Southern Ocean meridional overturning circulation as diagnosed from an eddy permitting state estimate, 2008.

Mazloff, M. R., Heimbach, P., and Wunsch, C.: An Eddy-Permitting Southern Ocean State Estimate, Journal of Physical Oceanography, 40, 880 – 899, https://doi.org/10.1175/2009JPO4236.1, 2010.

McKee, D. C., Yuan, X., Gordon, A. L., Huber, B. A., and Dong, Z.: Climate impact on interannual variability of Weddell Sea Bottom Water, Journal of Geophysical Research: Oceans, 116, https://doi.org/https://doi.org/10.1029/2010JC006484, 2011.

Meredith, M. P., Locarnini, R. A., Van Scoy, K. A., Watson, A. J., Heywood, K. J., and King, B. A.: On the sources of Weddell Gyre Antarctic Bottom Water, Journal of Geophysical Research: Oceans, 105, 1093–1104, https://doi.org/https://doi.org/10.1029/1999JC900263, 2000.

Meredith, M. P., Garabato, A. C. N., Gordon, A. L., and Johnson, G. C.: Evolution of the Deep and Bottom Waters of the Scotia Sea, Southern Ocean, during 1995–2005, Journal of Climate, 21, 3327 – 3343, https://doi.org/10.1175/2007JCLI2238.1, 2008.

Meredith, M. P., Gordon, A. L., Naveira Garabato, A. C., Abrahamsen, E. P., Huber, B. A., Jullion, L., and Venables, H. J.: Synchronous intensification and warming of Antarctic Bottom Water outflow from the Weddell Gyre, Geophysical Research Letters, 38, https://doi.org/https://doi.org/10.1029/2010GL046265, 2011.

Mohrmann, M., Heuzé, C., and Swart, S.: Southern Ocean polynyas in CMIP6 models, The Cryosphere, 15, 4281–4313, https://doi.org/10.5194/tc-15-4281-2021, 2021.

Mohrmann, M., Swart, S., and Heuzé, C.: Observed Mixing at the Flanks of Maud Rise in the Weddell Sea, Geophysical Research Letters, 49, e2022GL098 036, https://doi.org/https://doi.org/10.1029/2022GL098036, e2022GL098036 2022GL098036, 2022.

Morrison, A. K., Griffies, S. M., Winton, M., Anderson, W. G., and Sarmiento, J. L.: Mechanisms of Southern Ocean Heat Uptake and Transport in a Global Eddying Climate Model, Journal of Climate, 29, 2059 – 2075, https://doi.org/10.1175/JCLI-D-15-0579.1, 2016.

Nakata, K., Ohshima, K. I., and Nihashi, S.: Mapping of Active Frazil for Antarctic Coastal Polynyas, With an Estimation of Sea-Ice Production, Geophysical Research Letters, 48, e2020GL091 353, https://doi.org/https://doi.org/10.1029/2020GL091353, e2020GL091353 2020GL091353, 2021.

Naveira Garabato, A. C., McDonagh, E. L., Stevens, D. P., Heywood, K. J., and Sanders, R. J.: On the export of Antarctic Bottom Water from the Weddell Sea, Deep Sea Research Part II: Topical Studies in Oceanography, 49, 4715–4742, https://doi.org/https://doi.org/10.1016/S0967-0645(02)00156-X, deep Ocean Ventilation Through Antarctic Intermediate Layers (DOV ETAIL), 2002.

Neme, J., England, M. H., and Hogg, A. M.: Seasonal and Interannual Variability of the Weddell Gyre From a High-Resolution Global Ocean-Sea Ice Simulation During 1958–2018, Journal of Geophysical Research: Oceans, 126, e2021JC017 662, https://doi.org/https://doi.org/10.1029/2021JC017662, e2021JC017662 2021JC017662, 2021.

Nikurashin, M. and Vallis, G.: A Theory of Deep Stratification and Overturning Circulation in the Ocean, Journal of Physical Oceanography, 41, 485 – 502, https://doi.org/10.1175/2010JPO4529.1, 2011.

Nikurashin, M. and Vallis, G.: A Theory of the Interhemispheric Meridional Overturning Circulation and Associated Stratification, Journal of Physical Oceanography, 42, 1652 – 1667, https://doi.org/10.1175/JPO-D-11-0189.1, 2012.

Nycander, J., Hieronymus, M., and Roquet, F.: The nonlinear equation of state of sea water and the global water mass distribution, Geophysical Research Letters, 42, 7714–7721, https://doi.org/https://doi.org/10.1002/2015GL065525, 2015.

Orsi, A., Johnson, G., and Bullister, J.: Circulation, mixing, and production of Antarctic Bottom Water, Progress in Oceanography, 43, 55–109, https://doi.org/https://doi.org/10.1016/S0079-6611(99)00004-X, 1999.

Purkey, S. G. and Johnson, G. C.: Warming of Global Abyssal and Deep Southern Ocean Waters between the 1990s and 2000s: Contributions to Global Heat and Sea Level Rise Budgets*, Journal of Climate, 23, 6336–6351, 2010.

Purkey, S. G. and Johnson, G. C.: Global Contraction of Antarctic Bottom Water between the 1980s and 2000s, Journal of Climate, 25, 5830 – 5844, https://doi.org/10.1175/JCLI-D-11-00612.1, 2012.

Purkey, S. G. and Johnson, G. C.: Antarctic Bottom Water Warming and Freshening: Contributions to Sea Level Rise, Ocean Freshwater Budgets, and Global Heat Gain, Journal of Climate, 26, 6105 – 6122, https://doi.org/10.1175/JCLI-D-12-00834.1, 2013.

Purkey, S. G., Smethie, W. M., Gebbie, G., Gordon, A. L., Sonnerup, R. E., Warner, M. J., and Bullister, J. L.: A Synoptic View of the

745   Ventilation and Circulation of Antarctic Bottom Water from Chlorofluorocarbons and Natural Tracers, Annual Review of Marine Science, 10, 503–527, https://doi.org/10.1146/annurev-marine-121916-063414, pMID: 28877009, 2018.

Robertson, R., Visbeck, M., Gordon, A. L., and Fahrbach, E.: Long-term temperature trends in the deep waters of the Weddell Sea, Deep Sea Research Part II: Topical Studies in Oceanography, 49, 4791–4806, https://doi.org/https://doi.org/10.1016/S0967-0645(02)00159-5, deep Ocean Ventilation Through Antarctic Intermediate Layers (DOV ETAIL), 2002.

750   Small, R. J., Bacmeister, J., Bailey, D., Baker, A., Bishop, S., Bryan, F., Caron, J., Dennis, J., Gent, P., Hsu, H.-m., Jochum, M., Lawrence, D., Muñoz, E., diNezio, P., Scheitlin, T., Tomas, R., Tribbia, J., Tseng, Y.-h., and Vertenstein, M.: A new synoptic scale resolving global climate simulation using the Community Earth System Model, Journal of Advances in Modeling Earth Systems, 6, 1065–1094, https://doi.org/https://doi.org/10.1002/2014MS000363, 2014.

Stewart, A. L.: Mesoscale, tidal and seasonal/interannual drivers of the Weddell Sea overturning circulation, Journal of Physical Oceanography,

755   https://doi.org/10.1175/JPO-D-20-0320.1, 2021.

Talley, L. D.: Closure of the Global Overturning Circulation Through the Indian, Pacific, and Southern Oceans: Schematics and Transports, Oceanography, issue$_v olume$,, 2013.

Talley, L. D., Reid, J. L., and Robbins, P. E.: Data-Based Meridional Overturning Streamfunctions for the Global Ocean, Journal of Climate, 16, 3213 – 3226, https://doi.org/10.1175/1520-0442(2003)016<3213:DMOSFT>2.0.CO;2, 2003.

760   Tesdal, J.-E. and Abernathey, R. P.: Drivers of Local Ocean Heat Content Variability in ECCOv4, Journal of Climate, 34, 2941 – 2956, https://doi.org/10.1175/JCLI-D-20-0058.1, 2021.

Vernet, M., Geibert, W., Hoppema, M., Brown, P. J., Haas, C., Hellmer, H. H., Jokat, W., Jullion, L., Mazloff, M., Bakker, D. C. E., Brearley, J. A., Croot, P., Hattermann, T., Hauck, J., Hillenbrand, C.-D., Hoppe, C. J. M., Huhn, O., Koch, B. P., Lechtenfeld, O. J., Meredith, M. P., Naveira Garabato, A. C., Nöthig, E.-M., Peeken, I., Rutgers van der Loeff, M. M., Schmidtko,

765   S., Schröder, M., Strass, V. H., Torres-Valdés, S., and Verdy, A.: The Weddell Gyre, Southern Ocean: Present Knowledge and Future Challenges, Reviews of Geophysics, 57, 623–708, https://doi.org/https://doi.org/10.1029/2018RG000604, 2019.

Walin, G.: On the relation between sea-surface heat flow and thermal circulation in the ocean, Tellus, 34, 187–195, https://doi.org/https://doi.org/3490.1982.tb01806.x, 1982.

Williams, R.: Ocean Subduction, Academic Press, Oxford, second edition edn., https://doi.org/https://doi.org/10.1016/B978-

770   012374473-9.00109-0, 2001.

Wunsch, C. and Heimbach, P.: Practical global ocean state estimation, Physica D: Nonlinear Phenomena, 230, 197–208, https://doi.org/10.1016/j.physd.2006.09.040, 2007.

Wunsch, C. and Heimbach, P.: Dynamically and Kinematically Consistent Global Ocean Circulation and Ice State Estimates, vol. 103, pp. 553–579, https://doi.org/10.1016/B978-0-12-391851-2.00021-0, 2013.

775   Zweng, M., Reagan, J., Antonov, J., and R.A. Locarnini, A.V. Mishonov, T. B. H. G. O. B. D. J. D. M. B.: World Ocean Atlas 2013, Volume 2: Salinity. S. Levitus, Ed., A. Mishonov Technical Ed.; NOAA Atlas NESDIS, 74, 39, 2013.